AIP | The Journal of Chemical Physics

Torsionally mediated spin-rotation hyperfine splittings at moderate to high J values in methanol

S. P. Belov, G. Yu. Golubiatnikov, A. V. Lapinov, V. V. Ilyushin, E. A. Alekseev, A. A. Mescheryakov, J. T. Hougen, and Li-Hong Xu

Citation: The Journal of Chemical Physics **145**, 024307 (2016); doi: 10.1063/1.4954941
View online: http://dx.doi.org/10.1063/1.4954941
View Table of Contents: http://scitation.aip.org/content/aip/journal/jcp/145/2?ver=pdfcov
Published by the AIP Publishing

THE JOURNAL OF CHEMICAL PHYSICS **145**, 024307 (2016)

Torsionally mediated spin-rotation hyperfine splittings at moderate to high *J* values in methanol

S. P. Belov,[1] G. Yu. Golubiatnikov,[1] A. V. Lapinov,[1] V. V. Ilyushin,[2] E. A. Alekseev,[2,3] A. A. Mescheryakov,[2] J. T. Hougen,[4,a)] and Li-Hong Xu[5]

[1]*Institute of Applied Physics of the Russian Academy of Sciences, 46 Ulyanov Street, 603950 Nizhny Novgorod, Russia*
[2]*Institute of Radio Astronomy of National Academy of Sciences of Ukraine, Chervonopraporna 4, 61002 Kharkov, Ukraine*
[3]*Quantum Radiophysics Department of V. N. Karazin Kharkiv National University, Svobody Square 4, 61022 Kharkov, Ukraine*
[4]*Sensor Science Division, National Institute of Standards and Technology, Gaithersburg, Maryland 20899-8441, USA*
[5]*Department of Physics and Centre for Laser, Atomic, and Molecular Sciences, University of New Brunswick, Saint John, New Brunswick E2L 4L5, Canada*

(Received 25 April 2016; accepted 13 June 2016; published online 13 July 2016)

This paper presents an explanation based on torsionally mediated proton-spin–overall-rotation interaction for the observation of doublet hyperfine splittings in some Lamb-dip sub-millimeter-wave transitions between ground-state torsion-rotation states of E symmetry in methanol. These unexpected doublet splittings, some as large as 70 kHz, were observed for rotational quantum numbers in the range of $J = 13$ to 34, and $K = -2$ to $+3$. Because they increase nearly linearly with J for a given branch, we confined our search for an explanation to hyperfine operators containing one nuclear-spin angular momentum factor I and one overall-rotation angular momentum factor J (i.e., to spin-rotation operators) and ignored both spin-spin and spin-torsion operators, since they contain no rotational angular momentum operator. Furthermore, since traditional spin-rotation operators did not seem capable of explaining the observed splittings, we constructed totally symmetric "torsionally mediated spin-rotation operators" by multiplying the E-species spin-rotation operator by an E-species torsional-coordinate factor of the form $e^{\pm ni\alpha}$. The resulting operator is capable of connecting the two components of a degenerate torsion-rotation E state. This has the effect of turning the hyperfine splitting pattern upside down for some nuclear-spin states, which leads to bottom-to-top and top-to-bottom hyperfine selection rules for some transitions, and thus to an explanation for the unexpectedly large observed hyperfine splittings. The constructed operator cannot contribute to hyperfine splittings in the A-species manifold because its matrix elements within the set of torsion-rotation A_1 and A_2 states are all zero. The theory developed here fits the observed large doublet splittings to a root-mean-square residual of less than 1 kHz and predicts unresolvable splittings for a number of transitions in which no doublet splitting was detected. *Published by AIP Publishing.* [http://dx.doi.org/10.1063/1.4954941]

I. INTRODUCTION

Beginning in 2012, the Nizhny Novgorod group began to disseminate privately their rather surprising observation of 30–70 kHz doublet splittings in the Lamb-dip spectra of certain E-species transitions in methanol in the submillimeter-wave region. These observations, together with a partial theoretical explanation of their J and K systematics, were presented formally in 2013.[1]

The observed doublet splittings were rather surprising for several reasons. (i) Methanol has no quadrupolar nuclei, so any hyperfine explanation requires the splittings to be due to magnetic interactions involving the nuclear spins of the four protons, and separations of 70 kHz seemed too large for such interactions. (ii) Only transitions between certain pairs of rotational states showed these splittings, whereas closely related transitions, connecting the same pair of states to slightly different partners, did not. In almost all cases, the rather symmetrical and otherwise structureless line shapes of the various singlet lines and doublet components showed no evidence of additional underlying structure. (iii) One aspect of early attempts to understand the regularities of the splitting vs no-splitting patterns involved postulating an unusual splitting of the torsion-rotation E states of methanol into two components. (iv) $\Delta F = 0$ and ± 1 selection rules indicated that hyperfine splitting patterns of E-state Q-branch lines of methanol potentially contain 14 components, rather than only one or two. For A-state Q-branch lines, even more components are predicted. Because of the difficulty in rationalizing some or all of the information above, a number of molecular spectroscopists, including one of the authors of the present paper, initially suspected that the observed splittings were most probably experimental artifacts, possibly caused by the high radiation fields associated with Lamb-dip observations.

a)Author to whom correspondence should be addressed. Electronic mail: jon.hougen@nist.gov. Tel: +1-301-975-2379. Fax: +1-301-869-5700.

Immediately after the report,[1] the Kharkov group sought to repeat the subset of Nizhny Novgorod measurements that fell in the operating region of the Kharkov Lamb-dip spectrometer. Their measurements in fact agreed exactly with the Nizhny Novgorod splitting patterns where a comparison was possible, and they further observed a number of new doublet splittings, thus demonstrating clearly that these unexpected splittings were molecular, rather than instrumental, in origin.

In this paper we give a possible explanation for these splittings, based entirely on torsionally mediated spin-rotation interaction. While the explanation is internally consistent, we cannot rule out other possible explanations at this time, because of: (i) the large number of possible parameters in the effective Hamiltonian, (ii) the unknown positions of various other hyperfine transitions underneath (or outside of) each measured doublet component, (iii) the difficulty of measuring the splittings to more than about three significant figures, and (iv) lack of application of the model to E levels of excited torsional states. In Sections II and III a brief description of the apparatus and Lamb-dip measurements in Nizhny Novgorod and Kharkov are given. In Section IV the necessary theory is presented. In Sections V and VI the fitting Hamiltonian and a comparison with experiment is given. Section VII contains a discussion of the present status of the problem and conclusions.

Hyperfine splittings in methanol were considered previously in the classic papers of Heuvel and Dymanus,[2,3] where a number of high-resolution measurements were presented,[2] and much of the necessary theory was developed.[3] A very recent paper by Coudert *et al.*[4] uses the results of Ref. 3 to set up a rather complete hyperfine Hamiltonian formalism and to compute numerically, using modern quantum chemistry techniques, many of the hyperfine interaction parameters occurring in that Hamiltonian. In addition, Coudert *et al.*[4] carried out least-squares fits of the hyperfine splittings in 12 low-J transitions to a spin-spin, spin-rotation, and spin-torsion hyperfine Hamiltonian containing a number of terms from their formalism. The present work differs from Ref. 4 by presenting an explanation for doublet splittings in higher-J transitions of methanol that depends on three spin-rotation operators not used in the low-J fits of Ref. 4.

II. APPARATUS AND MEASUREMENTS FROM NIZHNY NOVGOROD

The Nizhny Novgorod Lamb-dip spectrometer was designed mainly to carry out precise frequency measurements of molecular transitions for very high resolution spectroscopy and for radio-astronomy problems. It operates in the frequency range from 40 GHz to 500 GHz, with a resolution up to 5 or 10 kHz, a sensitivity up to 10^{-8} cm^{-1}, and a measurement accuracy up to 400 Hz. The block-diagram and other parameters of the spectrometer have been described in detail,[5] so we give here only a brief description of the spectrometer, focusing on the resolution and other aspects important for the present study.

The millimeter and sub-millimeter wave radiation source employed in the spectrometer is a line of backward wave oscillators (BWOs) that are phase and frequency stabilized to the harmonics of the output signal from the active multiplication chain (3 × 2 × 3), driven by a direct digital frequency synthesizer PTS6400 (10–6400 MHz).[6] The reference oscillator of the PTS6400 is phase locked to a rubidium frequency standard controlled by a GPS-12RG receiver signal having a short-term frequency stability Δf/f of about 10^{-10} and a long-term stability of about 10^{-12}. The Lamb dip appears at the center of the absorption line when the BWO radiation passes through the gas cell twice and forms a standing wave inside the cell. The forward-travelling and returning waves are separated from each other with wire-grid polarizers and a roof-top reflector located at the end of the gas cell. After separation, the returning wave radiation is directed to a liquid helium cooled QMC InSb bolometer.

Frequency modulation and second harmonic detection by a SR830 lock-in amplifier were employed in the measurements, with a modulation rate of 2–5 kHz and a frequency deviation depth of 10–40 kHz. The phase modulator with a frequency of 35 MHz (synchronizer reference channel) allowed us to modulate the BWO frequency inside the PLL. The half width of the Lamb-dip was 10–30 kHz (HWHM), at a pressure 0.2–1 mTorr (1 Torr = 133.322 Pa), which is about one order of magnitude lower than the Doppler width. More details about the frequency modulation and the Lamb-dip line profiles obtained by this technique are given elsewhere.[7] The PTS6400 frequency control code and data acquisition graphics code are both written in a LabVIEW environment. A General Purpose Interface Bus communication card and a National Instruments data acquisition board are used.

The line width of the Lamb dip depends on many factors, including pressure broadening, power saturation, depth and frequency of the modulation, time of flight, divergence of the radiation beam, quality of the phase front of the radiation, and the level of some uncontrolled reflections into the cell. In the optimum limit, the line width is determined by the time of flight, which is in turn determined by the diameter of the beam, which may be as large as the gas cell.

The main source of line position uncertainty is due to some systematic shift caused by interference between signal from the line and reflected signal from cell windows, detector, etc., or the baseline influence. To minimize systematic error each line was measured many times for different pressures (0.2–1.5 mTorr), different power, and different positions on the baseline. These measurements showed that in our case typical scattering of the line center frequency due to its position on the base line is about 0.5–1.5 kHz, which exceeds the line-center uncertainties obtained from individual line profile analyses. In the case of overlapping lines in the saturated absorption regime, additional line frequency uncertainties arise from interference between lines.

Figure 1(a) shows, as an example, the $16_{-1} \leftarrow 15_{-2}$ transition between E species levels of methanol, which is split into a doublet with a separation of 36 kHz. Figure 1(b) shows how this doublet splitting can be precisely measured by carrying out a line-profile analysis. The half-width at half-maximum (HWHM) of the Lorentz profile used to model each component of the doublet is about 34 kHz, which is somewhat larger than HWHMs obtained for comparable

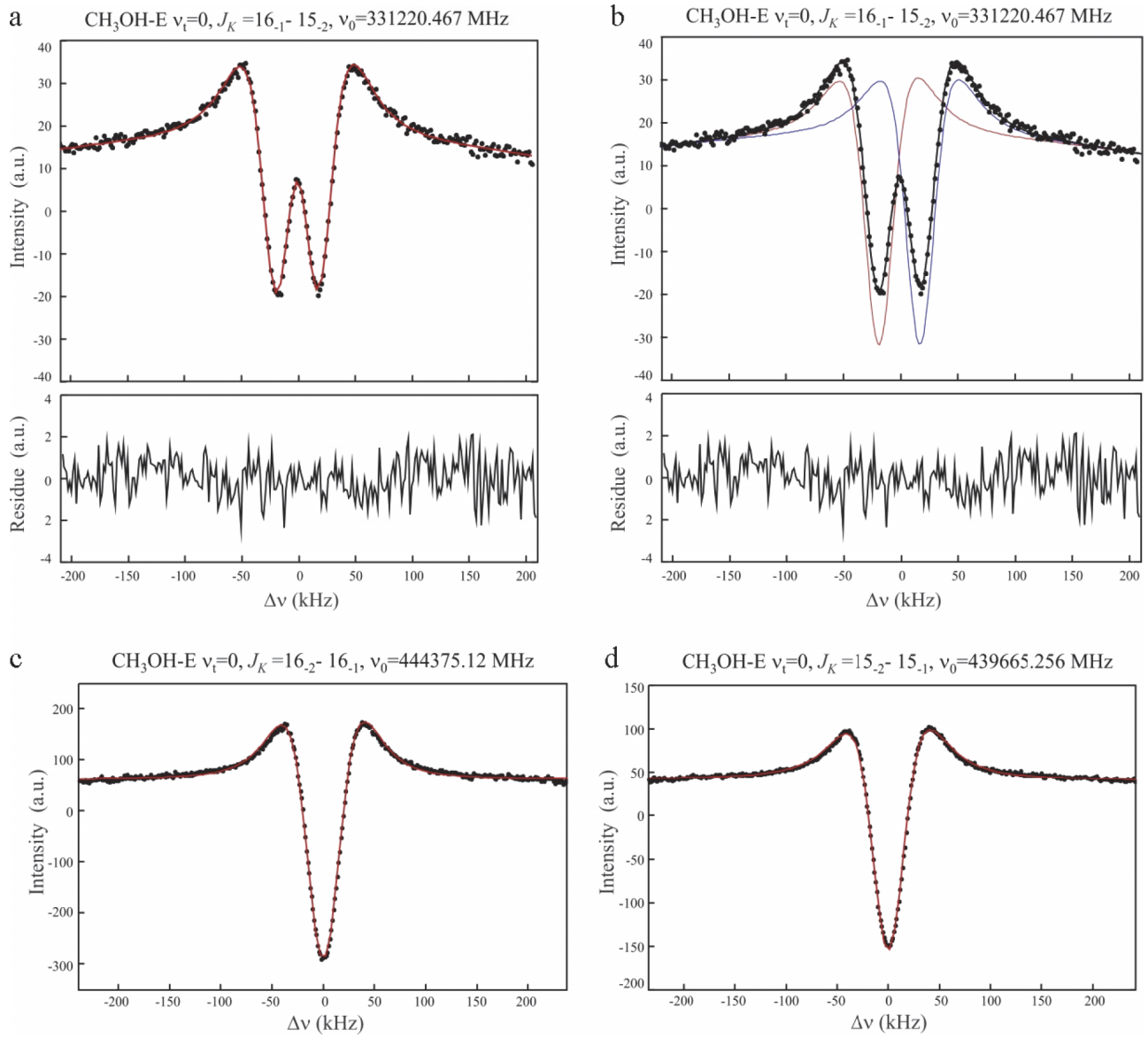

FIG. 1. (a) Observed Lamb-dip spectrum (solid black points) and fitted curve (red) from a line-profile analysis of the $16_{-1} \leftarrow 15_{-2}$ transition in the E species levels of methanol. (b) Line profile analysis of the Lamb-dip spectrum in (a), which assumes two Lamb-dip Lorentz components of equal intensity and equal width on an underlying Doppler profile, as detected with frequency modulation. The central frequency of the $16_{-1} \leftarrow 15_{-2}$ transition is $\nu_0 = 331\,220.467$ MHz; the frequencies of the doublet components are $\nu_1 = 331\,220.447$ MHz and $\nu_2 = 331\,220.483$ MHz. The splitting is 36 kHz, and the HWHM of each component is $\Delta\nu = 34$ kHz. In the bottom trace of (a) and (b) the residual from this line-profile analysis is shown. (c) Observed lack of doublet splitting in the $16_{-2} \leftarrow 16_{-1}$ transition ($\nu_0 = 444\,375.120$ MHz, $\Delta\nu = 33$ kHz) and (d) in the $15_{-2} \leftarrow 15_{-1}$ transition ($\nu_0 = 439\,665.256$ MHz, $\Delta\nu = 35$ kHz) of the E species levels of methanol. These transitions involve both the upper and lower state levels of the split transition shown in (a) and (b). The HWHM values of the Lorentz profiles for these two quite symmetrical lines are approximately equal to that of each doublet component in (a), suggesting that these lines are indeed singlets, or else are doublets with a very small doublet splitting (see Section VI C).

measurements on CO.[5,7] (Note that 34 kHz HWHM for the Lorentz profile corresponds to about 30 kHz FWHM for the line in second derivative display.) Figures 1(c) and 1(d) show the $15_{-2} \leftarrow 15_{-1}$ and $16_{-2} \leftarrow 16_{-1}$ transitions in the E species levels of methanol, which together involve both the upper and lower state levels of the split transition in Figure 1(a), but which nevertheless each appear as a single Lamb-dip line. The HWHM values for these two quite symmetrical lines are essentially the same as the HWHM of each component of the doublet in Figure 1(a). Most of the lines investigated in Nizhny Novgorod appear as singlets or doublets, but some lines have a more complex structure, as illustrated in Figure 2. The approximate 1:2:1 intensity ratio in this triplet could in principle arise from two equal-intensity doublets with a center spacing equal to the doublet splitting, i.e., could arise from an unresolved doublet of doublets.

III. APPARATUS AND MEASUREMENTS FROM KHARKOV

Measurements in Kharkov were carried out using a recently built Lamb-dip spectrometer that covers the frequency range from 50 to 150 GHz.[8] The spectrometer is built according to a commonly used approach, where a roof-top mirror is used to rotate the polarization by 90° at one end of the absorbing cell, and a wire-grid polarizer is used to separate the

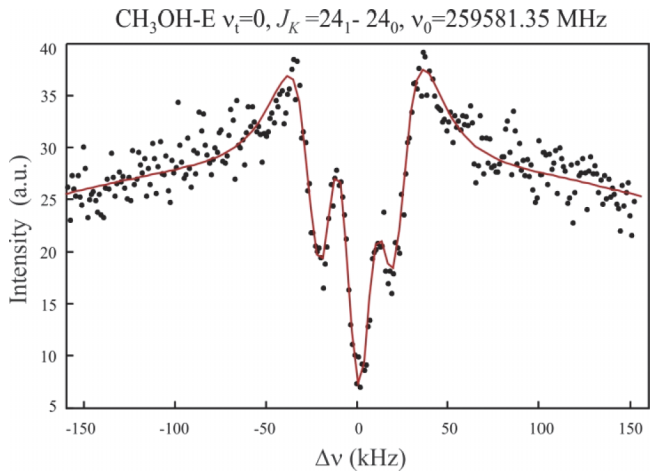

FIG. 2. Illustration of an apparent triplet structure in the splitting components. Such triplets were observed occasionally. They have not been treated theoretically in the present work, but we speculate that they might arise from an unresolved doublet of doublets, with the inner pair of lines overlapped. The line-profile fit (red line) gives a center frequency of $\nu_0 = 259\,581.350$ MHz, and frequencies for the three triplet components of $\nu_1 = 259\,581.330$ MHz, $\nu_2 = 259\,581.351$ MHz, and $\nu_3 = 259\,581.369$ MHz.

backward and forward waves at the other end.[9] The radiation source and the detector system of the spectrometer are essentially the same as described previously for the "parent" millimeter wave spectrometer from the Kharkov laboratory[10] with the exception of the modulation system. The spectrometer operates with a frequency modulated radiation source and a first harmonic lock-in detection system. Previously the minimum possible value of the modulation frequency was 10 kHz, which acted as the resolution limiting factor for the Lamb-dip measurements. To reduce this limiting factor to a negligible level a new modulation system was designed, based on a direct digital synthesizer that allows modulation frequencies down to 1 kHz or less to be used (details for this new modulation system can be found in Ref. 8).

Spectral resolution and measurement accuracy of the Kharkov Lamb-dip spectrometer were tested by recording the J = 1–0 transition of CO. Measurements were carried out in a glass-tube cell of 5.6 cm internal diameter and 300 cm long. The sample pressure during the measurements was much less than 1 mTorr. Our measurement of 115 271.2019 ± 0.0005 MHz for the CO J = 1–0 transition frequency, as well as the 10 kHz full width at half maximum (FWHM) of the Lamb-dip contour estimated for the second derivative are in a very good agreement with the corresponding Nizhny Novgorod results.[1,11] This same good agreement is observed for the doublet splittings of the five methanol transitions that were independently measured in both Kharkov and Nizhny Novgorod. For example, the Kharkov measurement for the splitting of the $v_t = 0, 27_{0,27} \leftarrow 27_{-1,27}$, E-type line at 104 853 MHz, is 72.7 kHz, in agreement with the Nizhny Novgorod measurement of 70.5 kHz.[1] As mentioned in the introduction, this good agreement between Lamb-dips measured with two quite different instruments in two different laboratories makes it nearly certain that these frequencies arise from properties of the molecule, rather than from properties of the spectrometers.

Figure 3 shows an example of measurements from the Kharkov Lamb-dip spectrometer (including some used to confirm the Nizhny Novgorod measurements). In this figure a series of E-type $v_t = 0$ Q-branch transitions with $K_a = 0 \leftarrow -1$ for the J range from 24 to 28 is presented. Each of these lines shows a clear doublet structure, with a smoothly varying value of the splitting. In total more than 130 methanol transitions in the 50–150 GHz frequency range have been measured. Using our spectrometer we were able to resolve the splittings of about 20 transitions. Typical FWHM values for the Lamb-dips varied from about 25 kHz to about 100 kHz. The large FWHM values of 90–100 kHz were observed mainly at low J; they strongly suggest unresolved underlying structure in these lines. In the ground torsional state the splittings were resolved only for the E-type transitions, whereas several doublets were detected for A-type transitions in the second excited torsional state. Also an unusual quartet pattern was detected for the $7_{70} \leftarrow 6_{60}$ E-type transition of the first excited torsional state of methanol. This doublet of doublets is shown in Figure 4.

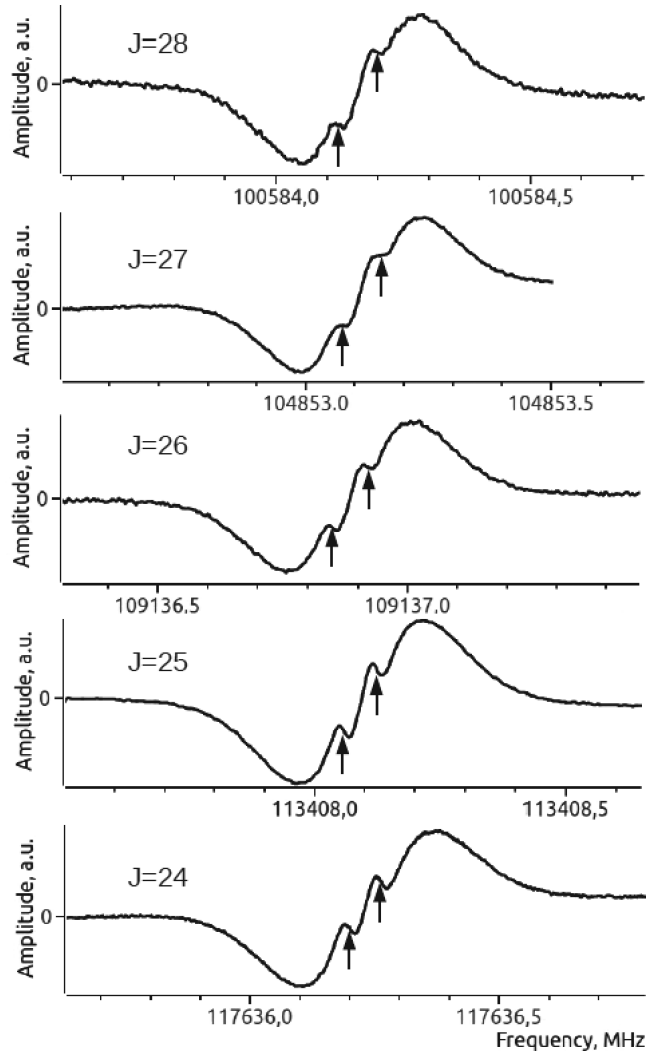

FIG. 3. Lamb-dips in the $K' = 0 \leftarrow K'' = -1$ Q branch of the E levels of methanol for the five transitions from $J = 24$ to $J = 28$, as measured in first-derivative display with the Kharkov spectrometer. The doublet splittings exhibit a smooth increase with J. The good agreement of three of these doublet splittings with earlier measurements of the same lines from the Nizhny Novgorod spectrometer convincingly demonstrates that these doublets are not instrumental artifacts.

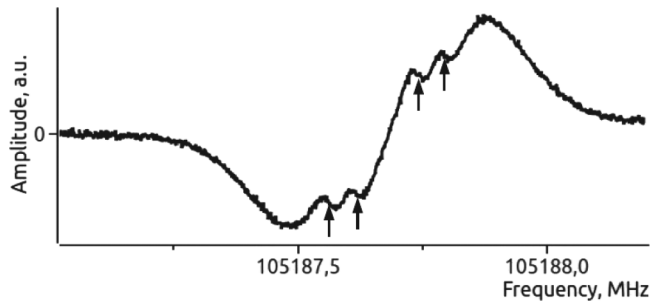

FIG. 4. Example of a quartet splitting pattern observed in the $7_{07} \leftarrow 6_{06}$ E line of the first excited torsional state, as recorded with the Kharkov spectrometer. Such quartet patterns are not treated in this paper, because their origin is not yet quantitatively understood, but some exploratory numerical calculations do give rise to hyperfine patterns with four strong components (at the resolution of the present experiments). The observation of this clear quartet pattern supports the conjecture that the triplet hyperfine pattern in Figure 2 is in fact a doublet of doublets with the two central components blended together.

IV. THEORY WHEN ONLY THE THREE METHYL PROTONS ARE TAKEN INTO ACCOUNT

To avoid confusion in what follows, we use one or more letters from the set *trs* as left superscripts on the symmetry species symbols Γ, on the wavefunctions Ψ, etc., to indicate quantities involving the methyl-torsion (t), the overall-rotation (r), and the nuclear-spin motion (s), respectively.

The present results preserve many of the features of the energy level diagrams and selection rules first presented by the Nizhny Novgorod group to explain their experimental observations, and one of the slides from Ref. 1 is presented here as Figure 5. The ^{tr}E levels in this figure are all shown as split into two components, labeled by + and −, which are assumed to alternate with K. By further assuming that P and R branch lines obey different selection rules on the ± labels than Q branch lines do, much of the observed pattern of doublet splittings versus no doublet splittings can be explained. Two aspects of this original explanation will be modified here. First, the ± labeling scheme in Figure 5 will be replaced by the C_{3v} symmetry species labels ${}^{trs}A_1$ and ${}^{trs}A_2$. With these labels the selection rules for P,Q,R lines become uniformly ${}^{trs}A_1 \leftrightarrow {}^{trs}A_2$. Second, the energy splittings in the torsion-rotation ^{tr}E levels of Figure 5 will become hyperfine splittings arising from differences in the sign of the spin-rotation coupling constant for ${}^{trs}A_1$ and ${}^{trs}A_2$ states.

A. Intuitive considerations and experimental findings

The torsion-rotation levels of methanol are well understood theoretically from earlier studies,[12] and "new" splittings of the ^{tr}E levels within the framework of the torsion-rotation Hamiltonian are not expected. Traditionally, the next level of splittings observed in closed-shell molecules arises from nuclear-electric-quadrupole and nuclear-magnetic-spin interactions. Since the $I = 0$ value for the nuclear spin of ^{12}C and ^{16}O, and the $I = ½$ value of the proton do not permit nuclear electric quadrupole moments, we assume in this paper that the newly observed splittings arise from nuclear spin-spin and/or nuclear spin-rotation interactions, both of which can give contributions to rotational energy levels of the order of tens of kHz.[13]

In methanol, we can combine a doubly degenerate torsion-rotation ^{tr}E wavefunction with a doubly degenerate nuclear-spin ^{s}E wavefunction to obtain four torsion-rotation-spin wavefunctions, belonging to the species ${}^{tr}E \otimes {}^{s}E = {}^{trs}A_1 \oplus {}^{trs}A_2 \oplus {}^{trs}E$. The Pauli exclusion principle immediately removes the ^{trs}E states from consideration. Because the other two species are allowed for fermions in methanol, we now have a mechanism to split the ^{tr}E level into two ^{trs}A states, similar to what has been depicted in Fig. 5. If the ${}^{trs}A_1$ and ${}^{trs}A_2$ states have qualitatively different nuclear spin interactions (which turns out in the present treatment to come from a sign change in the expectation values for

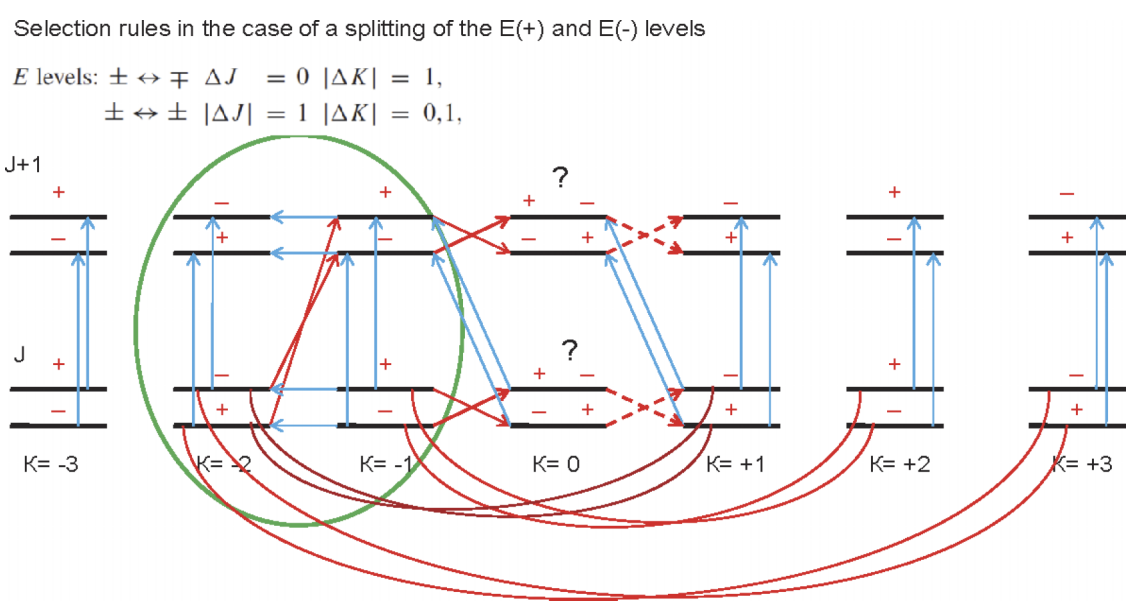

FIG. 5. A diagram of ^{tr}E level splittings taken from Ref. 1, which together with the indicated selection rules explains many of the experimental observations of doublet splittings versus no doublet splittings in the extensive Nizhny Novgorod measurements. This figure gives a very useful starting point for the present treatment.

some hyperfine operators), we might also have a mechanism for explaining some of the alternation in J and K of the splitting vs no-splitting patterns depicted in the power point presentation of Ref. 1.

It is known[4] that a rather large number of spin-rotation, spin-spin, and spin-torsion operators are allowed by group theory for an internally rotating methanol molecule. If precise quantum chemistry calculations of the coefficients for all terms involving nuclear spin operators were available, one could start by considering only the terms predicted to be large. Some calculations of this type have recently become available for methanol, but their precision is not yet fully established.[4]

We can gain experimental insight into which terms might be large by examining the experimental doublet splittings shown in Figure 6. Splittings within a given branch can be seen to increase roughly linearly with J. We expect that spin-spin splittings (arising from the product of two nuclear spin angular momenta)[3,4] and spin-torsion splittings (arising from the product of one nuclear spin angular momentum and the torsional angular momentum)[3,4] will not increase with J value. On the other hand, spin-rotation splittings (arising from the product of one nuclear spin angular momentum and the total angular momentum)[3,4] are known to increase approximately linearly with J. We thus assume that spin-spin and spin-torsion interactions can be ignored and concentrate on selecting appropriate terms for our effective hyperfine Hamiltonian from among the group-theoretically allowed spin-rotation operators.

B. Group theory applied to the nuclear spin operators

We follow the ideas and notation of an earlier work,[14] so that the character table used here for the permutation-inversion (PI) group G_6 (isomorphic with C_{3v}) is given in Table VII, and transformation properties of the rotational, torsional, and small-amplitude vibrational coordinates are given in Table VIII of Ref. 14. Since nuclear spin operators are not discussed in Ref. 14, and since we often switch back and forth in the present treatment among spin-rotation operators containing: (i) laboratory-fixed X,Y,Z components of the nuclear spin operators of the protons, (ii) molecule-fixed

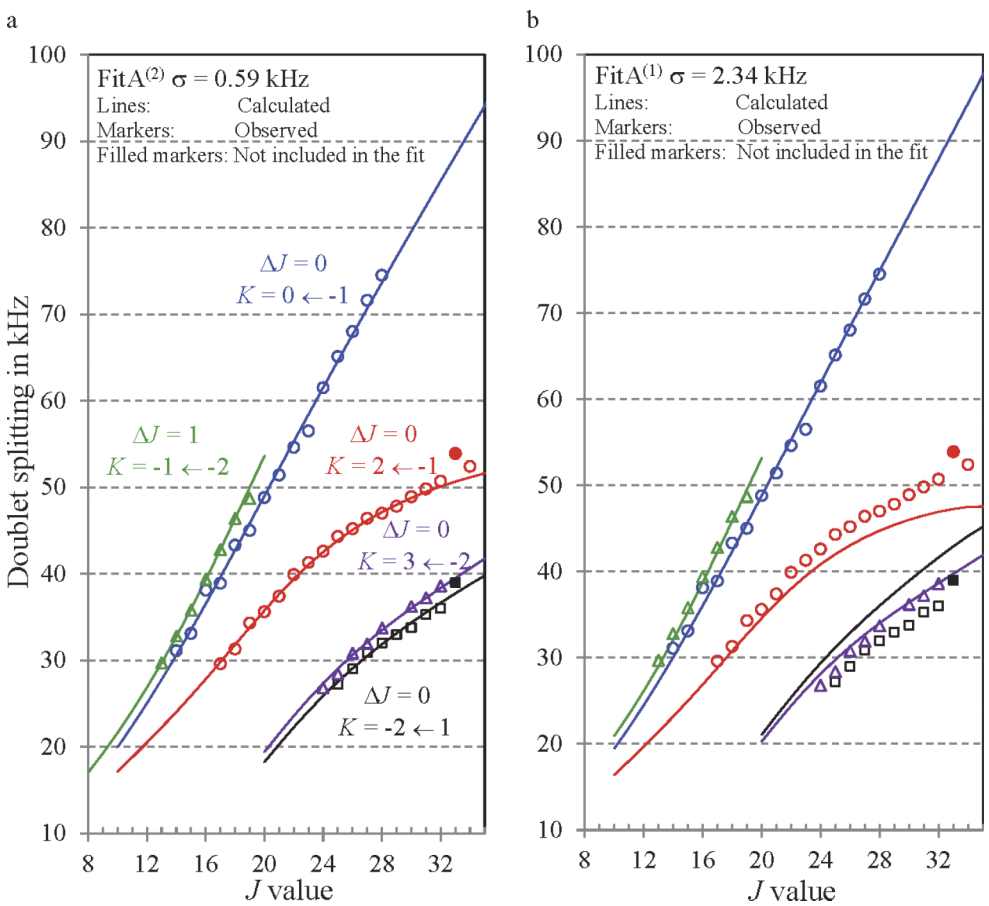

FIG. 6. (a) Observed (symbols) and calculated (solid curves) doublet splittings from FitA$^{(2)}$ in Table IV (see Section VI for details), plotted against the lower state J value. Different symbols are used to represent J lines belonging to different $K' - K''$ series, i.e. (from left to right): green Δ = the $K = -1 \leftarrow -2$ R branch, blue o = the $K = 0 \leftarrow -1$ Q branch, red o = the $K = +2 \leftarrow -1$ Q branch, purple Δ = the $K = +3 \leftarrow -2$ Q branch, and black □ = the $K = -2 \leftarrow +1$ Q branch. Calculated splittings have been extrapolated to $J = 35$, which is five J values beyond the experimental data set in Ref. 12. Even this short extrapolation may be dangerous, however, because molecular parameters from Ref. 12 were used to determine the composition of torsion-rotation wavefunctions needed for the hyperfine calculations here, and any local perturbations of these torsion-rotation wavefunctions above $J = 30$ will not have been taken into account. Apart from two bad points (one filled circle and one filled square, both at $J = 33$) that were excluded from the fit, the agreement between observed and calculated splittings is quite good. (b) A similar plot of the same observed splittings (same symbols), but with the solid curves calculated from FitA$^{(1)}$ in Table IV. Agreement between theory and experiment is significantly worse than for FitA$^{(2)}$ in (a), as can be seen numerically from the four-fold increase in standard deviation of the fit, or visually from the fact that two calculated curves in the lower right of Figure 6(b) do not pass through a large number of observed points.

x,y,z components of these same operators, and (iii) linear combinations of these components with coefficients that may or may not depend on the torsional angle α, it is useful to avoid confusion by specifying in some detail the symmetry properties of all members of this large collection of operators.

Since the laboratory-fixed components of the vector operator $\boldsymbol{I}_{\mathrm{H}}$ representing the spin of the OH proton are invariant to all feasible permutation-inversion operations in methanol, i.e., since they are invariant to all operations in the PI group G_6, all three laboratory-fixed components of $\boldsymbol{I}_H$ are of species A_1 in G_6, and transform like J_X, J_Y, J_Z in Table VII of Ref. 14.

Molecule-fixed and laboratory-fixed components are related to each other via the direction-cosine matrix S(χ,θ,ϕ),[14] as shown in Eq. (1)

$$\begin{bmatrix} I_{Hx} \\ I_{Hy} \\ I_{Hz} \end{bmatrix} = \left[S^{+1}(\chi,\theta,\varphi)\right] \begin{bmatrix} I_{HX} \\ I_{HY} \\ I_{HZ} \end{bmatrix}. \tag{1}$$

The molecule-fixed components on the left of Eq. (1) transform like J_x, J_y, J_z in Table VII,[14] i.e., they belong to the species A_2, A_1, and A_2 in G_6, respectively.

Symmetry species of the individual vector operators $\boldsymbol{I}_1$, $\boldsymbol{I}_2$, $\boldsymbol{I}_3$ (representing the spins of the CH_3 protons) cannot be defined in G_6, because these vectors are permuted among themselves by the operations in G_6. It is thus convenient to define three linear combinations of these vector operators (using constant coefficients chosen from the three cube roots of unity), which do have definite symmetry species in G_6

$$\begin{bmatrix} \mathbf{I}_{A1} \\ \mathbf{I}_{E+} \\ \mathbf{I}_{E-} \end{bmatrix} = \begin{bmatrix} 1 & 1 & 1 \\ 1 & e^{-2\pi i/3} & e^{+2\pi i/3} \\ 1 & e^{+2\pi i/3} & e^{-2\pi i/3} \end{bmatrix} \begin{bmatrix} \mathbf{I}_1 \\ \mathbf{I}_2 \\ \mathbf{I}_3 \end{bmatrix}. \tag{2}$$

The three laboratory-fixed components of $\boldsymbol{I}_{\mathrm{A1}}$ in Eq. (2) are each of species A_1 in G_6. The molecule-fixed components therefore transform like those of $\boldsymbol{I}_{\mathrm{H}}$ above (i.e., like J_x, J_y, J_z in Table VII of Ref. 14). It is the two operators $\boldsymbol{I}_{\mathrm{E}\pm}$ that will contribute to our explanation of the observed doublet splittings in ^{tr}E states.

The laboratory-fixed X components (or Y components, or Z components) of the pair of operators ($\boldsymbol{I}_{\mathrm{E}+}$, $\boldsymbol{I}_{\mathrm{E}-}$) are of species E in G_6. Their transformation matrices under the generators (123) and (23)* of G_6 are given (in the phase conventions of Ref. 14) by

$$(123)\begin{bmatrix} (I_{E+})_X \\ (I_{E-})_X \end{bmatrix} = \begin{bmatrix} e^{+2\pi i/3} & 0 \\ 0 & e^{-2\pi i/3} \end{bmatrix} \begin{bmatrix} (I_{E+})_X \\ (I_{E-})_X \end{bmatrix}, \tag{3}$$

$$(23)^*\begin{bmatrix} (I_{E+})_X \\ (I_{E-})_X \end{bmatrix} = \begin{bmatrix} 0 & 1 \\ 1 & 0 \end{bmatrix} \begin{bmatrix} (I_{E+})_X \\ (I_{E-})_X \end{bmatrix}. \tag{4}$$

Making use of the analogs of Eq. (1), it can be shown that the molecule-fixed x components (or y components, or z components) of ($\boldsymbol{I}_{\mathrm{E}+}$, $\boldsymbol{I}_{\mathrm{E}-}$) are also of species E in G_6. Transformations under (123) are given by Eq. (3) with X replaced by x, y, or z, respectively. Transformation of the y component under (23)* is given by Eq. (4) with X replaced by y. Transformation of the x (or z) component under (23)* is given by Eq. (5) (or Eq. (5) with x replaced by z)

$$(23)^*\begin{bmatrix} (I_{E+})_x \\ (I_{E-})_x \end{bmatrix} = \begin{bmatrix} 0 & -1 \\ -1 & 0 \end{bmatrix} \begin{bmatrix} (I_{E+})_x \\ (I_{E-})_x \end{bmatrix}. \tag{5}$$

Finally, it is useful to define two additional linear combinations of $\boldsymbol{I}_1$, $\boldsymbol{I}_2$, $\boldsymbol{I}_3$, which belong to non-degenerate symmetry species in G_6. They are less convenient to deal with than ($\boldsymbol{I}_{\mathrm{E}+}$, $\boldsymbol{I}_{\mathrm{E}-}$) when matrix elements are being computed because their coefficients depend on the torsional angle α, but they are more convenient to deal with when symmetry-allowed spin-rotation operators are being constructed. These linear combinations, which will be used below to construct *torsionally mediated* spin-rotation operators, are denoted by the slightly cumbersome notation $\boldsymbol{I}_{\mathrm{EA1}}$ and $\boldsymbol{I}_{\mathrm{EA2}}$, where the first subscript E indicates that they are related to the nuclear-spin operators of species E in Eq. (2), while the additional subscripts A_1 and A_2 indicate their actual symmetry in G_6. These two operators are defined in the following:

$$\begin{bmatrix} \mathbf{I}_{A1} \\ \mathbf{I}_{EA1} \\ \mathbf{I}_{EA2} \end{bmatrix} = \begin{bmatrix} 1 & 1 & 1 \\ \cos(\alpha) & \cos(\alpha + \frac{2\pi}{3}) & \cos(\alpha - \frac{2\pi}{3}) \\ \sin(\alpha) & \sin(\alpha + \frac{2\pi}{3}) & \sin(\alpha - \frac{2\pi}{3}) \end{bmatrix} \begin{bmatrix} \mathbf{I}_1 \\ \mathbf{I}_2 \\ \mathbf{I}_3 \end{bmatrix}. \tag{6}$$

C. Group theory applied to the torsion-rotation-nuclear-spin basis functions

If we define basis functions represented by the symbols $|E_+\rangle$ and $|E_-\rangle$ to transform according to Eqs. (3) and (4) regardless of what their left superscripts may be, then we find that the following functions

$$|^{trs}A_1\rangle = (1/\sqrt{2})[|^{tr}E_+\rangle|^{s}E_-\rangle + |^{tr}E_-\rangle|^{s}E_+\rangle], \tag{7a}$$

$$|^{trs}A_2\rangle = (1/\sqrt{2})[|^{tr}E_+\rangle|^{s}E_-\rangle - |^{tr}E_-\rangle|^{s}E_+\rangle], \tag{7b}$$

$$|^{trs}E_+\rangle = |^{tr}E_-\rangle|^{s}E_-\rangle, \tag{7c}$$

$$|^{trs}E_-\rangle = |^{tr}E_+\rangle|^{s}E_+\rangle, \tag{7d}$$

belong to the G_6 symmetry species $^{trs}A_1$, $^{trs}A_2$, $^{trs}E_+$, and $^{trs}E_-$, respectively. The ^{trs}E functions in Eqs. (7c) and (7d) are Pauli-forbidden and are thus of no interest. Note that Eq. (7) contains no *trs* wavefunctions built upon ^{tr}A states, since we only consider, in this paper, hyperfine splittings for ^{tr}E states.

The energy contribution from a hyperfine-interaction term H_{hf} to the Pauli-allowed states in Eq. (7a) or (7b) is given by an expectation value of the form $\langle^{trs}A_1|H_{hf}|^{trs}A_1\rangle$ or $\langle^{trs}A_2|H_{hf}|^{trs}A_2\rangle$. Non-zero cross terms between basis functions $|^{tr}E_+\rangle|^{s}E_-\rangle$ and $|^{tr}E_-\rangle|^{s}E_+\rangle$ on the right of Eq. (7) will clearly change sign when expectation values are calculated for the $^{trs}A_1$ and $^{trs}A_2$ functions on the left. This can cause much larger than expected nuclear-spin–overall-rotation splittings, because the $^{trs}A_1 \leftrightarrow {}^{trs}A_2$ electric-dipole selection rules will then lead to "bottom-to-top" and "top-to-bottom" transitions with respect to the hyperfine patterns of the upper and lower rotational states of a given asymmetric-rotor transition. To agree with the experimentally observed J and K alternation between large splittings and no splittings,[1] appropriate $(-1)^J$, $(-1)^{Ka}$, and/or $(-1)^{Kc}$ factors multiplying this sign change will, of course, also have to emerge from the theory.

Consider now transformation properties of the individual parts of a total *trs* basis function. The pair of torsional basis functions ($e^{+i\alpha}$, $e^{-i\alpha}$), as well as the pair ($e^{-2i\alpha}$, $e^{+2i\alpha}$), are both (^{t}E$_+$, ^{t}E$_-$) functions transforming[14] according to Eqs. (3) and (4) above. In many fitting programs based on effective torsion-rotation Hamiltonians for methanol, the degenerate torsional eigenfunctions after a matrix diagonalization are represented by basis-set sums of the form

$$|^tE_+\rangle = \Sigma_k A_k e^{+i(3k+1)\alpha}, \tag{8a}$$

$$|^tE_-\rangle = \Sigma_k A_k e^{-i(3k+1)\alpha}, \tag{8b}$$

where the summation index k ranges over all positive, zero, and negative integers with magnitude less than some k_{max}, and where the symbol on the left of the equality gives the symmetry in G$_6$ of this torsional eigenfunction. In Ref. 12 only eigenvalues and eigenfunctions for Eq. (8a) are actually computed. Eigenfunctions for Eq. (8b) are constructed here using the (23)* operation[14] and Eq. (4).

Asymmetric-top rotational basis functions also have a definite species in G$_6$. Using the Condon and Shortley phases adopted in Ref. 14 and using the principal axes ↔ molecule-fixed axes labeling convention (a, b, c) ↔ (z, x, y), we write (using standard $|J_{Ka,Kc}\rangle$ asymmetric-top notation on the left, and standard $|J, K_a, M_J\rangle$ symmetric-top notation on the right, with $K_a > 0$)

$$|J_{Ka,J-Ka}\rangle = (1/\sqrt{2})[|J, K_a, M_J\rangle + |J, -K_a, M_J\rangle], \tag{9a}$$

$$|J_{Ka,J-Ka+1}\rangle = (1/\sqrt{2})[|J, K_a, M_J\rangle - |J, -K_a, M_J\rangle]. \tag{9b}$$

These rotational functions are of species ^{r}A$_1$ and ^{r}A$_2$ in G$_6$ for even and odd K_c values, respectively. There are no rotational functions of species ^{r}E. The asymmetric-top quantum numbers K_a and K_c are well defined in this basis set, but they will not remain well defined in the torsion-rotation eigenfunctions of methanol, since asymmetric-rotor mixings and/or torsion-rotation mixings are often large. The quantum number M_J is frequently omitted in treatments of the torsion-rotation problem when external fields are absent; we retain M_J in some of the present equations because we want to couple M_J with the space-fixed projection M_I of the OH and/or CH$_3$ proton-spin angular momentum operators.

The discussion of symmetry species for nuclear-spin basis functions is less complicated than that for nuclear-spin operators, because we only consider nuclear-spin basis functions labeled by laboratory-fixed projections of the spin. Complications associated with the double group appropriate for treating half-integral spins, when rotations in the laboratory are considered, do not arise in the present work, because operations of the PI group G$_6$ do not involve any such rotations; they involve only permutations of identical particles and inversion of the laboratory-fixed coordinates.

The two components of the I = ½ nuclear spin function of the OH proton $|I_H = ½, M_H = \pm½\rangle$, are both of species A$_1$, since they are unaffected by any permutation of hydrogen atoms within the methyl group and by the laboratory-fixed inversion.

For the CH$_3$ protons, three basis functions having a spin projection of M_{CH3} = +½ can be written as $|M_1, M_2, M_3\rangle = |-½, +½, +½\rangle$, $|+½, -½, +½\rangle$, and $|+½, +½, -½\rangle$. Linear combinations of these M_{CH3} = +½ basis functions belonging to a given symmetry species in G$_6$ can be constructed as

$$\begin{bmatrix} |+1/2\rangle_{A1} \\ |+1/2\rangle_{E+} \\ |+1/2\rangle_{E-} \end{bmatrix} = \begin{bmatrix} 1 & 1 & 1 \\ 1 & e^{-2\pi i/3} & e^{+2\pi i/3} \\ 1 & e^{+2\pi i/3} & e^{-2\pi i/3} \end{bmatrix} \begin{bmatrix} |-1/2\rangle, & +1/2\rangle, & +1/2\rangle \\ |+1/2\rangle, & -1/2\rangle, & +1/2\rangle \\ |+1/2\rangle, & +1/2\rangle, & -1/2\rangle \end{bmatrix}. \tag{10}$$

Direct application of the operator $\boldsymbol{I}^2 \equiv (\boldsymbol{I}_1 + \boldsymbol{I}_2 + \boldsymbol{I}_3)^2$ shows that $|+½\rangle_{A1}$ has a total nuclear spin $I = 3/2$, while $|+½\rangle_{E+}$ and $|+½\rangle_{E-}$ have I = ½. M_{CH3} = −½ functions (though not necessarily satisfying Condon and Shortley phases) can be constructed by exchanging +½ and −½ values at all positions in the first and third matrices in Eq. (10).

One can construct two types of Pauli-allowed total wavefunctions (necessarily of species ^{trs}A$_1$ or ^{trs}A$_2$). The most familiar scheme, represented symbolically by ^{tr}E ⊗ ^{s}E, is to follow the energy ordering of the interactions and first construct ^{tr}E torsion-rotation functions and then combine them with ^{s}E proton spin functions. This scheme is most informative when ±K torsion-rotation splittings in the ^{tr}E state are larger than asymmetric-rotor splittings. (These two splittings are driven by the operators $-2F\rho P_\alpha J_z$ and $(1/2)(B - C)(J_x{}^2 - J_y{}^2)$, respectively.[14]) The second scheme, represented symbolically by (^{ts}A$_1$ ⊕ ^{ts}A$_2$) ⊗ (^{r}A$_1$ ⊕ ^{r}A$_2$), has the advantage of almost immediately getting rid of the complications of twofold degeneracies by combining the ^{t}E and ^{s}E functions to form non-degenerate torsion-spin functions and then multiplying these torsion-spin functions by ordinary asymmetric-rotor functions, which all belong to non-degenerate symmetry species. This scheme is most informative when ±K torsion-rotation splittings in the ^{tr}E state are smaller than asymmetric-rotor splittings. It is also the easiest scheme in which to search for symmetry-allowed spin-rotation operators that might give rise to the doublet splitting patterns under discussion here.

D. Construction of symmetry-allowed spin-rotation operators and their operator equivalents

Magnetic hyperfine coupling in a methyl group undergoing internal rotation has been discussed for methanol[3,4] and methyl formate.[15] We use here many ideas from Refs. 3, 4, and 15, many axis and phase conventions from Ref. 15, and some ideas from a paper on electric quadrupole coupling in an internally rotating CD$_3$ group.[16] Differences arise, however, because: (i) the axis system of Ref. 3 is different from ours, (ii) the quadrupole interactions of Ref. 16 do not map exactly onto the spin interactions here, and (iii) the authors of Ref. 15 placed their main emphasis on levels of ^{tr}A species, with $I_{CH3} = 3/2$, since no hyperfine splittings were observed for ^{tr}E levels in methyl formate. In contrast, we focus entirely on the ^{tr}E levels of methanol, with the simplification of a smaller total methyl-top spin of $I_{CH3} = 1/2$, but with the complication of a twofold torsional degeneracy.

The molecule-fixed axis system and hydrogen atom numbering are as given in Figure 2 of Ref. 15 (after

replacement of the OCHO group by OH). Instead of starting from Eq. (1) of Ref. 15 as an expression for the spin-rotation operator H_{sr}, we simply indicate in Table I all operators that could potentially occur in H_{sr}, i.e., all operators that are: (i) bilinear in $\boldsymbol{I}_i$ and $\boldsymbol{J}$, (ii) of species A_1 in G_6, (iii) Hermitian, and (iv) invariant under time reversal. Spin-rotation operators are to be constructed by multiplying one molecule-fixed component of $\boldsymbol{J}$ (from the first column in Table I) by one molecule-fixed component of some linear combination of the $\boldsymbol{I}_i$ (from the second column), since we expect that products of different molecule-fixed components and different linear combinations will in general have different (molecule-dependent) coefficients in the effective spin-rotation Hamiltonian operator. As pointed out in Section IV B, the symmetry species of J_x, J_y, and J_z are A_2, A_1, and A_2, respectively. It is thus convenient to consider the three linear combinations of $\boldsymbol{I}_1$, $\boldsymbol{I}_2$, $\boldsymbol{I}_3$ given in Eq. (6), since these also belong to non-degenerate species of G_6. We find from Eq. (6) and the transformation in Eq. (1) that the nine molecule-fixed components of these three linear combinations belong to the species $4\,{}^{ts}A_1 \oplus 5\,{}^{ts}A_2$, where the left superscript *ts* indicates that some of the operators contain both a proton-spin and a torsional factor. We can now count the number of independent spin-rotation operators that arise only from the three methyl hydrogens by counting the number of ${}^{trs}A_1$ species that arise in the direct product

$$\Gamma(\boldsymbol{J}_{MOL}) \otimes \Gamma[(\boldsymbol{I}_1,\boldsymbol{I}_2,\boldsymbol{I}_3)_{MOL}] = ({}^{r}A_1 \oplus 2\,{}^{r}A_2) \otimes (4\,{}^{ts}A_1 \oplus 5\,{}^{ts}A_2) = 14\,{}^{trs}A_1 \oplus 13\,{}^{trs}A_2. \tag{11}$$

We can also determine the total number of spin-rotation operators that occur in H_{sr} by adding the ${}^{s}A_1 \oplus 2\,{}^{s}A_2$ species of the molecule-fixed components of the hydroxyl $\boldsymbol{I}_H$ to the second parentheses in Eq. (11) to obtain

TABLE I. Operators[a] that contribute independent terms[b] to the spin-rotation Hamiltonian[c] in methanol.

Rotational[d]	Nuclear-spin[e]	Group-theory[f]
J_x or J_z	I_{Hx} or I_{Hz}	${}^{r}A_2 \otimes {}^{ts}A_2$
	I_{A1x} or I_{A1z}	
	I_{EA1x} or I_{EA1z}	
	I_{EA2y}	
J_y	I_{Hy}	${}^{r}A_1 \otimes {}^{ts}A_1$
	I_{A1y}	
	I_{EA1y}	
	I_{EA2x} or I_{EA2z}	

[a]Operators consist of two factors, one chosen from the first column (rotational part) of the table, and one from the second column (nuclear spin part). Operators in each part are given in terms of their components along the molecule-fixed x, y, z axes.
[b]Each of these 19 ${}^{trs}A_1$ operators can have its own coefficient in the effective spin-rotation Hamiltonian, and this coefficient will differ for different molecules.
[c]This table lists all spin-rotation operators of species ${}^{trs}A_1$ found in the direct product shown in Eq. (12).
[d]The rotational operator which is to be multiplied by one of the nuclear-spin operators to generate a spin-rotation interaction term.
[e]A nuclear-spin operator from Eq. (6), which may also contain some torsional angle dependence.
[f]Symmetry species in G_6 of the rotational and nuclear-spin factors from the first and second columns of the table.

$$\Gamma(\boldsymbol{J}_{MOL}) \otimes \Gamma[(\boldsymbol{I}_1,\boldsymbol{I}_2,\boldsymbol{I}_3,\boldsymbol{I}_H)_{MOL}] = ({}^{r}A_1 \oplus 2\,{}^{r}A_2) \otimes (5\,{}^{ts}A_1 \oplus 7\,{}^{ts}A_2) = 19\,{}^{trs}A_1 \oplus 17\,{}^{trs}A_2. \tag{12}$$

It is these 19 symmetry-allowed ${}^{trs}A_1$ spin-rotation operators that we wish to construct from the information given in Table I. We note in passing that while it is possible to use operators in Table I containing one I factor, one J factor, and one torsional factor like $e^{\pm i\alpha}$, it is not possible to use operators consisting of one I factor, one J factor, and one P_α factor, since such operators are not invariant to time reversal.

If only matrix elements of the spin-rotation operators satisfying $\Delta J = 0$ are to be considered in the Hamiltonian, as is appropriate when hyperfine interactions are much smaller than rotational spacings (as in methanol), then the direction-cosine matrix in Eq. (1) can be replaced by its operator equivalent to give

$$\begin{bmatrix} I_{Hx} \\ I_{Hy} \\ I_{Hz} \end{bmatrix} = \frac{1}{J(J+1)} \begin{bmatrix} J_xJ_X & J_xJ_Y & J_xJ_Z \\ J_yJ_X & J_yJ_Y & J_yJ_Z \\ J_zJ_X & J_zJ_Y & J_zJ_Z \end{bmatrix} \begin{bmatrix} I_{HX} \\ I_{HY} \\ I_{HZ} \end{bmatrix}. \tag{13}$$

Eq. (13) allows all operators in Table I to be rewritten as illustrated by the following two examples:

$$(J_x)(I_{Hx}) = (I_{Hx})(J_x) = [1/J(J+1)]J_x^2(\boldsymbol{J}\cdot\boldsymbol{I}_H)_{LAB}, \tag{14a}$$

$$(J_x)(I_{EA1z}) + (I_{EA1z})(J_x) = [1/J(J+1)](J_xJ_z + J_zJ_x) \times (\boldsymbol{J}\cdot\boldsymbol{I}_{EA1})_{LAB}, \tag{14b}$$

where the subscript LAB means that the scalar product in the last set of parentheses is to be written using laboratory-fixed components of the two vector operators. This is an important point because matrix elements of components of $\boldsymbol{J}_{LAB}$ depend only on the quantum numbers J and M_J, and matrix elements of components of $(\boldsymbol{I}_H)_{LAB}$ or $(\boldsymbol{I}_{EA1})_{LAB}$ are conveniently calculated using nuclear spin functions with laboratory-fixed projection quantum numbers (as discussed in Section IV C).

E. Two illustrative spin-rotation interaction terms and their very different contributions to the spin-rotation energy

It is convenient to examine spin-rotation energy contributions from two types of operators occurring in H_{sr}, which we denote in shorthand notation by $H_{sr}^{(+)}$ and $H_{sr}^{(-)}$. Matrix elements of these operators have the properties

$$\langle {}^{trs}A_1 | H_{sr}^{(+)} | {}^{trs}A_1 \rangle = +\langle {}^{trs}A_2 | H_{sr}^{(+)} | {}^{trs}A_2 \rangle, \tag{15a}$$

$$\langle {}^{trs}A_1 | H_{sr}^{(-)} | {}^{trs}A_1 \rangle = -\langle {}^{trs}A_2 | H_{sr}^{(-)} | {}^{trs}A_2 \rangle, \tag{15b}$$

when the ${}^{trs}A_1$ and ${}^{trs}A_2$ functions are taken to be the two nuclear-spin components belonging to a given ${}^{tr}E$ level in methanol.

The first illustrative operator to be considered is of the type $H_{sr}^{(+)}$. It occurs in the hyperfine Hamiltonian for ordinary

asymmetric rotors and is given by the linear combination

$$C_1(J_xI_{A1x} + J_yI_{A1y} + J_zI_{A1z}) \rightarrow C_1[J_x^2(\boldsymbol{J}\cdot\boldsymbol{I}_{A1})_{LAB} + J_y^2(\boldsymbol{J}\cdot\boldsymbol{I}_{A1})_{LAB} + J_z^2(\boldsymbol{J}\cdot\boldsymbol{I}_{A1})_{LAB}]/J(J+1) = C_1(\boldsymbol{J}\cdot\boldsymbol{I}_{A1})_{LAB}, \quad (16)$$

where $\boldsymbol{I}_{A1}$ is defined in Eq. (6). The matrix element of this operator on both sides of the equality in Eq. (15a) is $+(1/2)C_1[F(F+1) - J(J+1) - I(I+1)]$. (Details of the calculations in this section are given in the supplementary material.[17]) Matrix elements of the type shown in Eq. (15a) cannot explain the observed splitting patterns under discussion here unless unexpectedly large changes (of the order of 50 or 100 kHz) are postulated for the C_1 values in the upper and lower states of the transition.

The second illustrative operator is of the type $H_{sr}^{(-)}$ and is given by a similar linear combination, but with I_{A1x} replaced by I_{EA1x}, etc., where $\boldsymbol{I}_{EA1}$ is also defined in Eq. (6),

$$C_2(J_xI_{EA1x} + J_yI_{EA1y} + J_zI_{EA1z}) \rightarrow C_2[J_x^2(\boldsymbol{J}\cdot\boldsymbol{I}_{EA1})_{LAB} + J_y^2(\boldsymbol{J}\cdot\boldsymbol{I}_{EA1})_{LAB} + J_z^2(\boldsymbol{J}\cdot\boldsymbol{I}_{EA1})_{LAB}]/J(J+1) = C_2(\boldsymbol{J}\cdot\boldsymbol{I}_{EA1})_{LAB}. \quad (17)$$

Its hyperfine matrix elements take the form[17]

$$\langle {}^{ts}A_1{}^rA_q \left| C_2(\boldsymbol{J}\cdot\boldsymbol{I}^{(1)}_{EA1})_{LAB}\right| {}^{ts}A_1{}^rA_q\rangle = -(1/2)C_2\langle {}^tE_+|e^{-i\alpha}|{}^tE_-\rangle \times [F(F+1) - J(J+1) - I(I+1)], \quad (18a)$$

$$\langle {}^{ts}A_2{}^rA_q \left| C_2(\boldsymbol{J}\cdot\boldsymbol{I}^{(1)}_{EA1})_{LAB}\right| {}^{ts}A_2{}^rA_q\rangle = +(1/2)C_2\langle {}^tE_+|e^{-i\alpha}|{}^tE_-\rangle \times [F(F+1) - J(J+1) - I(I+1)], \quad (18b)$$

where ${}^rA_q$ can be either asymmetric-rotor function in Eq. (9), with $q = p$ or $q = 3 - p$ and $p = (1/2)[3 - (-1)^{J-Ka}]$. Because of the α-dependence appearing in Eq. (18) (see Ref. 17 for the meaning of the superscript $^{(1)}$ on $\boldsymbol{I}_{EA1}$), these operators cannot occur in the hyperfine Hamiltonian for ordinary asymmetric rotors. To distinguish them from the "pure spin-rotation" operators in Eq. (16), we say that operators like those in Eq. (17) arise from "torsionally mediated spin-rotation interactions." Eq. (18) allows us to define[17] an effective spin-rotation coupling coefficient $C_{\rm eff}^{(1)}$, whose value is chosen so that a matrix element of the form $\langle I, J, F, M_F|\ C_{\rm eff}^{(1)}\ (\boldsymbol{J}\cdot\boldsymbol{I})_{\rm LAB}|I, J, F, M_F\rangle$ has the same value as the matrix element in Eq. (18). For basis functions involving $|{}^{ts}A_1\rangle$ and $|{}^{ts}A_2\rangle$ factors, $C_{\rm eff}^{(1)}$ is given by Eqs. (19a) and (19b), respectively,

$$C^{(1)}_{eff}({}^{ts}A_1) = -C_2\langle {}^tE_+|e^{-i\alpha}|{}^tE_-\rangle, \quad (19a)$$

$$C^{(1)}_{eff}({}^{ts}A_2) = +C_2\langle {}^tE_+\left|e^{-i\alpha}\right|{}^tE_-\rangle = -C^{(1)}_{eff}({}^{ts}A_1). \quad (19b)$$

Note that phase conventions for the ${}^tE_\pm$ functions have been fixed,[14] so that the sign of $C_{\rm eff}^{(1)}$ (${}^{ts}A_1$) is determined theoretically. It is not easily determined experimentally, however, because it is difficult to know which levels are ${}^{trs}A_1$ and which are ${}^{trs}A_2$.

F. Systematic organization of spin-rotation operators from Table I

As mentioned, only spin-rotation operators involving $\boldsymbol{I}_{\rm EA1}$ or $\boldsymbol{I}_{\rm EA2}$ in Table I give matrix elements of the form $H_{sr}^{(-)}$ in Eq. (15b), so we immediately exclude operators involving $\boldsymbol{I}_{\rm H}$ or $\boldsymbol{I}_{\rm A1}$. A total of nine $H_{sr}^{(-)}$ operators that are in addition Hermitian and of species ${}^{trs}A_1$ can be constructed from Table I. Six of these are of the form ${}^rA_2 \otimes {}^{ts}A_2$ and three of the form ${}^rA_1 \otimes {}^{ts}A_1$. When the direction cosines in these operators are replaced by their operator equivalents from Eq. (13) (an approximation that prevents calculation of any $\Delta J \neq 0$ hyperfine matrix elements), only six independent operators remain from these nine. They can conveniently be arranged as elements of two 3×3 matrices as follows:

$$H_{sr}^{(-)} = [J(J+1)]^{-1}\begin{bmatrix} J_x^2 & 0 & \frac{1}{2}\{J_x, J_z\} \\ 0 & J_y^2 & 0 \\ \frac{1}{2}\{J_x, J_z\} & 0 & J_z^2 \end{bmatrix}(\boldsymbol{I}_{\rm EA1}\cdot\boldsymbol{J})_{\rm LAB} + [J(J+1)]^{-1}\begin{bmatrix} 0 & \frac{1}{2}\{J_x, J_y\} & 0 \\ \frac{1}{2}\{J_x, J_y\} & 0 & \frac{1}{2}\{J_y, J_z\} \\ 0 & \frac{1}{2}\{J_y, J_z\} & 0 \end{bmatrix} \times (\boldsymbol{I}_{\rm EA2}\cdot\boldsymbol{J})_{\rm LAB}, \quad (20)$$

where here and below we use $(\boldsymbol{J}\cdot\boldsymbol{I}_{\rm EA1})_{\rm LAB} = (\boldsymbol{I}_{\rm EA1}\cdot\boldsymbol{J})_{\rm LAB}$ and $(\boldsymbol{J}\cdot\boldsymbol{I}_{\rm EA2})_{\rm LAB} = (\boldsymbol{I}_{\rm EA2}\cdot\boldsymbol{J})_{\rm LAB}$ to change to the conventional form for spin-rotation interaction operators. The operators used in our fitting Hamiltonian will be chosen from the matrices in Eq. (20).

V. THE FITTING HAMILTONIAN USED TO TREAT THE EXPERIMENTAL DATA

Arguments in the supplemental material suggest that it makes sense to try to explain the methanol doublet splittings observed in the present work in terms of a hyperfine spin-rotation Hamiltonian operator involving only the methyl protons. Furthermore, for the least-squares fits carried out in this paper, we consider only operators involving $({J_x}^2 + {J_y}^2)$, $({J_x}^2 - {J_y}^2)$, and $(J_xJ_y + J_yJ_x)$ in Eq. (20). Matrix elements of operators involving ${J_z}^2$ were found to give much smaller contributions because of the low K values of the experimentally observed splittings. Matrix elements of operators involving $(J_xJ_z + J_zJ_x)$ and $(J_yJ_z + J_zJ_y)$ were also small, because of the very small $\Delta K = \pm 1$ mixings in methanol (caused by the small value of D_{ab} in the torsion-rotation Hamiltonian).

A. Parameter definitions in the Hamiltonian for the least-squares fit

Modifying somewhat the notation in Eq. (8-43) of Ref. 13, we define (using the notation of Table I and Eqs. (S-4) and (S-5)) six real parameters in the effective spin-rotation Hamiltonian $H_{sr}^{(-)}$ under consideration here by the symbols $A_{ij}^{(1)}$ and $A_{ij}^{(2)}$,

$$H_{sr}^{(-)} = A_{xx}^{(1)} J_x I_{EA1x}^{(1)} + A_{yy}^{(1)} J_y I_{EA1y}^{(1)} + (1/2) A_{xy}^{(1)} \left(J_x I_{EA2y}^{(1)} + J_y I_{EA2x}^{(1)} + I_{EA2y}^{(1)} J_x + I_{EA2x}^{(1)} J_y \right)$$
$$+ A_{xx}^{(2)} J_x I_{EA1x}^{(2)} + A_{yy}^{(2)} J_y I_{EA1y}^{(2)} + (1/2) A_{xy}^{(2)} \left(J_x I_{EA2y}^{(2)} + J_y I_{EA2x}^{(2)} + I_{EA2y}^{(2)} J_x + I_{EA2x}^{(2)} J_y \right). \quad (21)$$

These A_{ij} parameters are generalized versions of the C_2 parameter used in Eq. (17) to define the $H_{sr}^{(-)}$ interaction term in the simplified spin-rotation Hamiltonian of Section IV E.

As described in the supplemental material,[17] we modify the Hamiltonian in Eq. (21) in several ways to obtain the Hamiltonian operator that is actually used in our least-squares fits. First, the direction cosines implicitly contained in the molecule-fixed components of $\boldsymbol{I}_{\mathrm{EA1}}$ and $\boldsymbol{I}_{\mathrm{EA2}}$ via Eq. (1) are replaced by their operator equivalents in Eq. (13) to give analogs of the operator following the arrow in Eq. (17):

$$H_{sr}^{(-)} = [(A_{xx}^{(1)} J_x^2 + A_{yy}^{(1)} J_y^2)(\boldsymbol{I}_{EA1}^{(1)} \cdot \boldsymbol{J})_{LAB} + A_{xy}^{(1)} \left(J_x J_y + J_y J_x \right) (\boldsymbol{I}_{EA2}^{(1)} \cdot \boldsymbol{J})_{LAB}]/J\,(J+1)$$
$$+ [(A_{xx}^{(2)} J_x^2 + A_{yy}^{(2)} J_y^2)(\boldsymbol{I}_{EA1}^{(2)} \cdot \boldsymbol{J})_{LAB} + A_{xy}^{(2)} \left(J_x J_y + J_y J_x \right) (\boldsymbol{I}_{EA2}^{(2)} \cdot \boldsymbol{J})_{LAB}]/J\,(J+1). \quad (22)$$

Next the α-dependence implicit in the operators $\boldsymbol{I}_{\mathrm{EA1}}{}^{(1,2)}$ and $\boldsymbol{I}_{\mathrm{EA2}}{}^{(1,2)}$ via Eqs. (6), (S-4), and (S-5) is explicitly written, the resulting $\boldsymbol{I}_{\mathrm{E}\pm}$ operators are replaced by their operator equivalents in Eq. (S-8), and expectation values are taken in the final coupled *trs* eigenfunctions to obtain expressions analogous to Eqs. (18a) and (18b),

$$\langle {}^{trs}A_1; I, J, F, M_F \left| H_{sr}^{(-)} \right| {}^{trs}A_1; I, J, F, M_F \rangle = \{[A_{xx}^{(1)} \langle J_x^2 \rangle^{(1)} + A_{yy}^{(1)} \langle J_y^2 \rangle^{(1)} + A_{xy}^{(1)} i \langle J_x J_y + J_y J_x \rangle^{(1)}$$
$$+ A_{xx}^{(2)} \langle J_x^2 \rangle^{(2)} + A_{yy}^{(2)} \langle J_y^2 \rangle^{(2)} + A_{xy}^{(2)} i \langle J_x J_y + J_y J_x \rangle^{(2)}]/J(J+1)\}$$
$$\times (-1/2)[F\,(F+1) - J\,(J+1) - I\,(I+1)], \quad (23a)$$

$$\langle {}^{trs}A_2; I, J, F, M_F \left| H_{sr}^{(-)} \right| {}^{trs}A_2; I, J, F, M_F \rangle = -\langle {}^{trs}A_1; I, J, F, M_F \left| H_{sr}^{(-)} \right| {}^{trs}A_1; I, J, F, M_F \rangle. \quad (23b)$$

The four quantities $-A_{xx}{}^{(1,2)} \langle J_x{}^2 \rangle^{(1,2)}/J(J+1)$ and $-A_{yy}{}^{(1,2)} \langle J_y{}^2 \rangle^{(1,2)}/J(J+1)$ are close analogs of the $C_{\mathrm{eff}}{}^{(1)}$ parameter defined in connection with Eq. (19), but they differ from $C_{\mathrm{eff}}{}^{(1)}$ because they involve expectation values calculated with respect to numerical torsion-rotation eigenvectors obtained from a fit of $v_t = 0$, 1, and 2 methanol transitions and they thus vary with both J and K, as described in Sec. V B. The two quantities $-A_{xy}{}^{(1,2)} i \langle J_x J_y + J_y J_x \rangle^{(1,2)}/J(J+1)$ are more distant analogs of $C_{\mathrm{eff}}{}^{(1)}$, because matrix elements of the Hermitian operators $(J_x J_y + J_y J_x)$ and $(\boldsymbol{I}_{\mathrm{EA2}}{}^{(1,2)} \cdot \boldsymbol{J})_{\mathrm{LAB}}$ in Eq. (22) are all pure imaginary in the basis set used here. Expectation values of the product operators actually occurring in $H_{sr}{}^{(-)}$ of Eq. (22) are all real, however, as shown in the supplementary material[17] (and as required for a Hermitian Hamiltonian operator).

B. Numerical calculation of torsion-rotation matrix elements like $\langle J_x{}^2 \rangle^{(1)}$ using ^{tr}E wavefunctions obtained from a global fit of the methanol microwave and far infrared data

The three real expectation values written in shorthand notation as $\langle J_x{}^2 \rangle^{(1)}$, $\langle J_y{}^2 \rangle^{(1)}$, and $i \langle J_x J_y + J_y J_x \rangle^{(1)}$ in Eq. (23) can be shown to have the form

$$\langle J_x^2 \rangle^{(1)} = +\langle {}^{tr}E_+ \left| e^{-i\alpha} J_x^2 \right| {}^{tr}E_- \rangle$$
$$= (1/4) \langle {}^{tr}E_+ \left| e^{-i\alpha} (2\boldsymbol{J}^2 - 2J_z^2 + J_+^2 + J_-^2) \right| {}^{tr}E_- \rangle, \quad (24a)$$

$$\langle J_y^2 \rangle^{(1)} = (1/4) \langle {}^{tr}E_+ \left| e^{-i\alpha} (2\boldsymbol{J}^2 - 2J_z^2 - J_+^2 - J_-^2) \right| {}^{tr}E_- \rangle, \quad (24b)$$

$$i \langle J_x J_y + J_y J_x \rangle^{(1)} = (1/2) \langle {}^{tr}E_+ \left| e^{-i\alpha} (J_+^2 - J_-^2) \right| {}^{tr}E_- \rangle, \quad (24c)$$

where the ladder operators $J_\pm \equiv J_x \pm i J_y$ have real and positive matrix elements in the $|K, J, M\rangle$ basis set. The corresponding quantities with right superscript $^{(2)}$ can be obtained from Eq. (24) by replacing[17] α by -2α. Eq. (24) can be derived most easily by taking matrix elements in Eq. (23) using the $M_F = F$ wavefunction of the $F = J + 1/2$ manifold,[17] since this wavefunction contains only one uncoupled basis function, namely, that with $M_I = I = ½$ and $M_J = J$, and by taking ^{trs}A$_1$ and ^{trs}A$_2$ wavefunctions in the form given in Eqs. (7a) and (7b), respectively.

To evaluate the integrals in Eq. (24), we constructed ^{tr}E$_+$ torsion-rotation wavefunctions of methanol from computer-program output associated with the final fit given in Ref. 12. For the BELGI program used there, this procedure required using numerical eigenvector coefficients from the second-step diagonalization to generate linear combinations of eigenvectors from the first-step diagonalization that give eigenvector coefficients in the |free-rotor⟩|symmetric-top⟩ basis set. Each resulting ^{tr}E$_+$ wavefunction then consisted of numerical entries in a partitioned column vector belonging to a given torsion-rotation energy, a given J, and a given value of $\sigma = +1$. The basis-set quantum number labelling the large blocks of each partitioned column vector is the rotational projection K along the RAM z axis, and runs from $K = -J$ to $K = +J$. The quantum number labelling functions within each block is the exponent of the torsional factor in Eq. (8) and runs from $m \equiv 3k + \sigma = 3k + 1 = -29$ to $m \equiv 3k + 1 = +31$ in steps of 3 (since σ is set to +1 in the program, and k runs from −10 to +10 in increments of unity). These column vectors contain numerical values for the $A_{K,k}$ coefficients appearing in Eqs. (25) and (26) below.

TABLE II. Example matrix elements for the torsion-rotation operators in Eq. (28), as illustrated in Eq. (26).

Operator[a]	Symbol[b]	$J_K = 20_{-2}$[c]	$J_K = 21_{-2}$[c]	$J_K = 21_{-1}$[c]
$e^{-i\alpha} J_x{}^2/J(J+1)$	$\langle J_x{}^2\rangle^{(1)}/J(J+1)$	0.379 83	−0.420 29	−0.046 08
$e^{-i\alpha} J_y{}^2/J(J+1)$	$\langle J_y{}^2\rangle^{(1)}/J(J+1)$	0.125 00	−0.141 86	−0.390 67
$e^{-i\alpha} J_z{}^2/J(J+1)$	$\langle J_z{}^2\rangle^{(1)}/J(J+1)$	0.003 95	−0.003 95	−0.001 00
$e^{-i\alpha}\{iJ_x, J_y\}/J(J+1)$	$i\,\langle J_xJ_y + J_yJ_x\rangle^{(1)}/J(J+1)$	0.130 80	−0.127 95	0.241 83
$e^{+2i\alpha} J_x{}^2/J(J+1)$	$\langle J_x{}^2\rangle^{(2)}/J(J+1)$	0.349 86	−0.383 49	0.069 05
$e^{+2i\alpha} J_y^2/J(J+1)$	$\langle J_y^2\rangle^{(2)}/J(J+1)$	0.035 97	−0.047 57	−0.440 34
$e^{+2i\alpha} J_z{}^2/J(J+1)$	$\langle J_z{}^2\rangle^{(2)}/J(J+1)$	0.002 85	−0.002 85	−0.000 85
$e^{+2i\alpha}\{iJ_x, J_y\}/J(J+1)$	$i\,\langle J_xJ_y + J_yJ_x\rangle^{(2)}/J(J+1)$	0.258 36	−0.268 63	0.456 52

[a]Exact form of various torsion-rotation operators with $\Delta m = -1$ and $\Delta m = +2$ torsional selection rules, as discussed in Section V.
[b]Shorthand symbols for matrix elements of these operators, as used in Eqs. (23) and (28).
[c]J and signed K quantum number labels for three example ^{tr}E levels. Columns under these labels contain numerical values, for use in Eq. (28), of the matrix elements shown on the left, which were calculated as illustrated in Eqs. (24) and (26), using numerical torsion-rotation eigenvectors of methanol (i.e., $A_{K,k}$ coefficients) taken from the large global fit described in Ref. 12 (see text).

Wavefunctions belonging to the same energy, same ^{tr}E symmetry, and same J value, but with $\sigma = -1$, i.e., the $|^{tr}\mathrm{E}_-\rangle$ eigenfunctions, were generated by applying the symmetry operation (23)* of Ref. 14, according to the following equation:

$$(23)^*\left[\Sigma_{K,k}A_{K,k}\left|e^{+i(3k+1)\alpha}\right\rangle\left|K,J,M_J\right\rangle/\sqrt{2}\pi\right] = \Sigma_{K,k}(-1)^{J-K}A_{K,k}\left|e^{+i(-3k-1)\alpha}\right\rangle\left|-K,J,M_J\right\rangle/\sqrt{2}\pi. \tag{25}$$

Matrix elements of various operators between the two degenerate components of a given ^{tr}E state were then calculated as indicated by the two following examples:

$$\langle {}^{tr}E_+\left|e^{+2i\alpha}J_z^2\right|{}^{tr}E_-\rangle = \Sigma_{K,k}(A_{K,k})(A_{-K,-k})\,(-1)^{J-K}\,K^2, \tag{26a}$$

$$\langle {}^{tr}E_+\left|e^{-i\alpha}J_+^2\right|{}^{tr}E_-\rangle = \Sigma_{K,k}(A_{K,k})\,(A_{-K-2,-k-1})\,(-1)^{J-K} \times[(J-K)(J+K+1) \times(J-K-1)(J+K+2)]^{1/2}. \tag{26b}$$

Table II gives numerical examples of these matrix elements for the ^{tr}E states of methanol with $J_K = 20_{-2}$, 21_{-2}, and 21_{-1}. There are no sign ambiguities in this table, since $|^{tr}\mathrm{E}_+\rangle$ and $|^{tr}\mathrm{E}_-\rangle$ phases are related by Eq. (25). Relatively small changes in the magnitude of the matrix elements occur when changing J from 20_{-2} to 21_{-2}, whereas relatively large changes occur in changing K from 21_{-2} to 21_{-1}. For these three levels, matrix elements of the $^{(1)}$ and $^{(2)}$ operators in Table II tend to track each other. This behavior suggests that observed doublet splittings for a large number of spectral branch types may be required to establish convincingly whether it is better to use operators with superscript $^{(1)}$ or $^{(2)}$ in the fits.[17] The matrix elements given in Table II were used in the final fits of Sec. VI.

VI. COMPARISON OF THEORY WITH EXPERIMENT

The experimentally observed data can be divided into three groups: (i) clearly resolved doublets, with a well measured doublet splitting, (ii) unsplit single lines, where an unmeasurable doublet splitting could take any value from zero up to almost the full line width, and (iii) a few lines with contours suggesting an underlying triplet or quartet structure. Since the dataset of resolved splittings for the ground torsional state of methanol considered in this work is overwhelmingly dominated by doublets, our strategy for testing the model Hamiltonian at this point is to include, in the least-squares fits, only well measured doublet splittings, and then to "predict" from the determined constants the splittings that are expected theoretically for the (unsplit) singlet lines.

Because we did not have a reliable prediction of whether first $^{(1)}$ or second $^{(2)}$ order Fourier expansion terms in the torsional functions should be more important, we carried out a number of least-squares fits[17] using the nuclear spin operators in Eqs. (S-4) and (S-5), both separately and together. It eventually became clear that we could not simultaneously determine all six A coefficients from the presently available experimental data. We thus present here fits using only the three $A^{(1)}$ coefficients or only the three $A^{(2)}$ coefficients. As mentioned, the $J_z{}^2$ term in Eq. (20) was not well determined (presumably because of the low K_a values of lines in the present data set), so this term was not used in our final fits.

The quantity Δ_{calc} used here for the theoretically calculated doublet splitting of a given torsion-rotation transition is specified by the following equation:

$$\Delta_{calc} \equiv \nu({}^{trs}A_2 \leftarrow {}^{trs}A_1; F = J + 1/2) - \nu({}^{trs}A_2 \leftarrow {}^{trs}A_1; F = J - 1/2) \tag{27a}$$

$$= \left[E'\left({}^{trs}A_2; F' = J' + 1/2\right) - E''\left({}^{trs}A_1; F'' = J'' + 1/2\right)\right] - \left[E'({}^{trs}A_2; F' = J' - 1/2) - E''({}^{trs}A_1; F'' = J'' - 1/2)\right]. \tag{27b}$$

Eq. (27a) says that we calculate all transition frequencies ν so that the upper state has overall symmetry $^{trs}\Gamma = \mathrm{A}_2$ and the lower state has symmetry $^{trs}\Gamma = \mathrm{A}_1$, and then we subtract a $F = J - 1/2$ frequency from a $F = J + 1/2$ frequency. (We note in passing that each of the two transitions in Eq. (27b) obeys the selection rule $\Delta F = \Delta J$.) Energies are taken from Eq. (23), so that the final expression for Δ_{calc} used to fit observed values of the doublet splittings becomes

$$\Delta_{calc} = [A^{(1)}_{xx}\langle J_x^2\rangle^{(1)} + A^{(1)}_{yy}\langle J_y^2\rangle^{(1)} + A^{(1)}_{xy}i\langle J_xJ_y + J_yJ_x\rangle^{(1)} + A^{(2)}_{xx}\langle J_x^2\rangle^{(2)} + A^{(2)}_{yy}\langle J_y^2\rangle^{(2)} + A^{(2)}_{xy}i\langle J_xJ_y + J_yJ_x\rangle^{(2)}]'(J'+1/2)/J'(J'+1) - [A^{(1)}_{xx}\langle J_x^2\rangle^{(1)} + A^{(1)}_{yy}\langle J_y^2\rangle^{(1)} + A^{(1)}_{xy}i\langle J_xJ_y + J_yJ_x\rangle^{(1)} + A^{(2)}_{xx}\langle J_x^2\rangle^{(2)} + A^{(2)}_{yy}\langle J_y^2\rangle^{(2)} + A^{(2)}_{xy}i\langle J_xJ_y + J_yJ_x\rangle^{(2)}]''(J''+1/2)/J''(J''+1), \quad (28)$$

where the $'$ and $''$ superscripts after the square brackets indicate that quantities like $\langle J_x{}^2\rangle^{(1)}$ (as defined in Eq. (24)) are to be calculated for the upper or lower torsion-rotation state, respectively, of the hyperfine transitions ν in Eq. (27a).

A. Sign ambiguities

The definition of Δ_{calc} in Eq. (27) causes it to take both positive and negative values, so we can only compare Δ_{calc} directly with experimental data if we know which doublet component contains each of the transitions specified in Eq. (27). There is, however, almost no hope of determining experimentally whether the higher energy component of a measured doublet contains the pair of unresolved transitions $\nu(^{trs}A_2 \leftarrow {}^{trs}A_1; F = J+ ½)$ and $\nu(^{trs}A_1 \leftarrow {}^{trs}A_2; F = J- ½)$ or contains the pair $\nu(^{trs}A_2 \leftarrow {}^{trs}A_1; F = J- ½)$ and $\nu(^{trs}A_1 \leftarrow {}^{trs}A_2; F = J+ ½)$ (see Figure S-1). The experimental measurements thus only provide values for $|\Delta_{obs}|$.

The fact that $|\Delta_{obs}| \geq 0$ for all measurements leads to two different sign difficulties in our fitting procedure. The

TABLE III. Results of 16 fits of the experimental doublet splittings[a] with different sign combinations.[b]

Branch[c]	$K' \leftarrow K''$[c]	#[d]	Sign1[e]	Sign2[e]	Sign3[e]	Sign4[e]	Sign5[e]	Sign6[e]	Sign7[e]	Sign8[e]
Q	$+2 \leftarrow -1$	17	+	+	+	+	+	+	+	+
Q	$0 \leftarrow -1$	15	+	−	+	+	+	−	−	−
R	$-1 \leftarrow -2$	7	+	+	−	+	+	−	+	+
Q	$-2 \leftarrow +1$	8	+	+	+	−	+	+	−	+
Q	$+3 \leftarrow -2$	8	+	+	+	+	−	+	+	−
σ_{fit}			14	12	4	12	20	14	14	13
$A^{(2)}{}_{xx}$			−34	−28	+5	−40	−33	+11	−34	−27
$A^{(2)}{}_{yy}$			+36	+77	+54	−2	+20	+95	+40	+62
$A^{(2)}{}_{xy}$			−42	−83	−20	−36	−26	−61	−77	−67
$A^{(1)}{}_{xx}$			+27	+24	−5	+31	+28	−8	+28	+25
$A^{(1)}{}_{yy}$			−16	−38	−43	+17	−6	−65	−5	−29
$A^{(1)}{}_{xy}$			+21	+43	−6	+38	+10	+16	+60	+33
Branch[c]	$K' \leftarrow K''$[c]	#[d]	Sign9[e]	Sign10[e]	Sign11[e]	Sign12[e]	Sign13[e]	Sign14[e]	Sign15[e]	Sign16[e]
Q	$+2 \leftarrow -1$	17	+	+	+	+	+	+	+	+
Q	$0 \leftarrow -1$	15	+	+	+	−	−	+	−	−
R	$-1 \leftarrow -2$	7	−	−	+	−	+	−	−	−
Q	$-2 \leftarrow +1$	8	−	+	−	−	−	−	+	−
Q	$+3 \leftarrow -2$	8	+	−	−	+	−	−	−	−
σ_{fit}			9	6	16	19	11	0.6	5	10
$A^{(2)}{}_{xx}$			−1	+6	−39	+5	−33	−0.1	+12	+6
$A^{(2)}{}_{yy}$			+16	+38	−17	+58	+24	+1.1	+80	+42
$A^{(2)}{}_{xy}$			−14	−4	−20	−55	−61	+2.5	−45	−39
$A^{(1)}{}_{xx}$			−0.6	−4	+32	−4	+29	+0.1	−7	−3
$A^{(1)}{}_{yy}$			−10	−33	+27	−32	+4	+0.1	−55	−22
$A^{(1)}{}_{xy}$			+10	−17	+27	+32	+49	−0.6	+5	+21

[a]The observed doublet splittings are grouped into five branches according to their ΔJ and $K'-K''$ values, since hyperfine splittings within the same branch are expected to have the same sign.

[b]We define the sign of the doublet splitting in a transition to be + when the $F = J + ½$ component lies above the $F = J - ½$ component. Since this cannot be determined experimentally, we arbitrarily take splittings in the $K = +2 \leftarrow -1Q$ branch to be positive and determine the signs of splittings in the other branches relative to this one.

[c]In this column the first five rows in each half of the table label the five branches of transitions by their ΔJ and ΔK values. Symbols in the last seven rows in each half of the table represent the standard deviation of the fit, and the six constants floated in the fit, all in kHz.

[d]The number of doublet splittings in each branch included in the fit.

[e]The five rows with signs in each of these columns indicate one of the 16 different sign combinations. The seven rows with numbers give numerical values for the symbols on the left, as obtained from each least-squares fit. Sign14 has a σ_{fit} and a set of spin-rotation coupling constants that are dramatically smaller than those in other columns. We thus believe that Sign14 represents the correct choice to use in our final least squares fit.

TABLE IV. Results of least-squares fits to Eq. (28) of observed doublet splittings in methanol.

Transition[a] J′K′ –J″K″	Frequency[b] in MHz	Δ_{obs}[c] in kHz	Lab[d]	wt[e]	FitA$^{(2)}$[f]	FitA$^{(1)}$[g]
17_2–17_{-1}	368 730.689	29.6	N	1	29.8	28.8
18_2–18_{-1}	373 005.999	31.3	N	1	31.8	30.8
19_2–19_{-1}	377 660.799	34.3	N	1	33.8	32.7
20_2–20_{-1}	382 672.564	35.6	N	1	35.8	34.6
21_2–21_{-1}	388 024.844	37.4	N	1	37.6	36.4
22_2–22_{-1}	393 709.927	39.9	N	1	39.4	38.0
23_2–23_{-1}	399 729.276	41.3	N	1	41.0	39.5
24_2–24_{-1}	406 092.081	42.6	N	1	42.5	40.8
25_2–25_{-1}	412 812.723	44.3	N	1	43.9	42.0
26_2–26_{-1}	419 908.000	45.2	N	1	45.1	43.1
27_2–27_{-1}	427 394.732	46.4	N	1	46.2	44.0
28_2–28_{-1}	435 288.026	47.0	N	1	47.1	44.7
29_2–29_{-1}	443 600.314	47.8	N	1	48.0	45.4
30_2–30_{-1}	452 341.136	48.9	N	1	48.8	46.0
31_2–31_{-1}	461 517.760	49.8	N	1	49.5	46.5
32_2–32_{-1}	471 137.118	50.7	N	1	50.1	46.9
33_2–33_{-1}	481 210.715	53.9	N	0	50.7	47.3
34_2–34_{-1}	491 768.522	52.4	N	1	51.1	47.5
14_0–14_{-1}	150 141.672	31.1	N	1	30.6	30.1
15_0–15_{-1}	148 111.993	33.1	N	1	33.5	33.0
16_0–16_{-1}	145 766.227	38.1	K,N	1	36.5	36.0
17_0–17_{-1}	143 108.385	38.9	K,N	1	39.6	39.2
18_0–18_{-1}	140 151.208	43.3	K	1	42.7	42.3
19_0–19_{-1}	136 915.288	45.0	K	1	45.9	45.6
20_0–20_{-1}	133 427.704	48.8	K	1	49.0	48.8
21_0–21_{-1}	129 720.384	51.4	K	1	52.2	52.1
22_0–22_{-1}	125 828.376	54.6	K	1	55.3	55.4
23_0–23_{-1}	121 788.194	56.5	K	1	58.4	58.6
24_0–24_{-1}	117 636.363	61.5	K	1	61.5	61.9
25_0–25_{-1}	113 408.222	65.1	K,N	1	64.6	65.2
26_0–26_{-1}	109 137.011	68.0	K,N	1	67.7	68.4
27_0–27_{-1}	104 853.237	71.6	K,N	1	70.7	71.7
28_0–28_{-1}	100 584.287	74.5	K	1	73.7	74.9
14_{-1}–13_{-2}	242 446.084	−29.7[h]	N	1	−29.7	−29.0
15_{-1}–14_{-2}	287 233.894	−32.8	N	1	−32.7	−32.1
16_{-1}–15_{-2}	331 220.371	−35.8	N	1	−36.0	−35.3
17_{-1}–16_{-2}	374 293.551	−39.4	N	1	−39.3	−38.7
18_{-1}–17_{-2}	416 339.136	−42.8	N	1	−42.8	−42.3
19_{-1}–18_{-2}	457 245.121	−46.4	N	1	−46.4	−45.9
20_{-1}–19_{-2}	496 907.359	−48.7	N	1	−50.0	−49.5
25_{-2}–25_1	155 548.487	−27.2[h]	N	1	−27.5	−31.2
26_{-2}–26_1	164 486.238	−29.0	N	1	−29.1	−32.9
27_{-2}–27_1	174 206.590	−30.9	N	1	−30.5	−34.5
28_{-2}–28_1	184 706.607	−32.0	N	1	−31.9	−36.0
29_{-2}–29_1	195 985.174	−33.0	N	1	−33.1	−37.5
30_{-2}–30_1	208 043.713	−33.8	N	1	−34.4	−38.9
31_{-2}–31_1	220 886.784	−35.3	N	1	−35.5	−40.3
32_{-2}–32_1	234 523.365	−36.0	N	1	−36.7	−41.6
33_{-2}–33_1	248 970.736	−39.0	N	0	−37.7	−42.9
24_3–24_{-2}	418 038.276	−26.8[h]	N	1	−27.3	−28.1
25_3–25_{-2}	412 353.296	−28.4	N	1	−29.0	−29.8
26_3–26_{-2}	406 336.912	−30.8	N	1	−30.6	−31.3
27_3–27_{-2}	400 047.723	−31.9	N	1	−32.1	−32.7
28_3–28_{-2}	393 544.800	−33.7	N	1	−33.5	−34.0
30_3–30_{-2}	380 123.328	−36.2	N	1	−36.0	−36.4

TABLE IV. (*Continued.*)

Transition[a] J′K′ –J″K″	Frequency[b] in MHz	Δ_{obs}[c] in kHz	Lab[d]	wt[e]	FitA$^{(2)}$[f]	FitA$^{(1)}$[g]
31_3–31_{-2}	373 307.399	−37.2	N	1	−37.2	−37.5
32_3–32_{-2}	366 480.506	−38.6	N	1	−38.4	−38.6

[a]Labeled by the upper (′) and lower (″) state J and signed K quantum numbers.
[b]Calculated center frequency of the doublet in MHz, as given in Ref. 12 or in the data base http://spec.jpl.nasa.gov/ftp/pub/catalog/catform.html.
[c]Observed splitting of the Lamb-dip doublets.
[d]Laboratory where the measurement was made. N = Nizhny Novgorod, K = Kharkov. When measurements were made in both laboratories, an average was taken.
[e]Weight of the measurement in the fit.
[f]Residuals from a fit using only three $A_{ij}^{(2)}$ constants in Eq. (28), i.e., from a fit with all $A_{ij}^{(1)} \equiv 0$. This fit has a standard deviation of 0.59 kHz.
[g]Residuals from a fit using only three $A_{ij}^{(1)}$ constants in Eq. (28), i.e., all $A_{ij}^{(2)} \equiv 0$. This fit has a standard deviation of 2.34 kHz.
[h]See Section VI A for the meaning of these negative splittings.

first arises because there is a $(-1)^J$ sign alternation in Δ_{calc}, as can be seen by comparing the 20_{-2} and 21_{-2} entries in Table II. We have chosen to handle this sign alternation with J by comparing values of $(-1)^{J''-1}\Delta_{calc}$ to values of $|\Delta_{obs}|$ in our least-squares routine, since values of $(-1)^{J''-1}\Delta_{calc}$ for the transitions considered here turn out to be either all positive or all negative for a given ΔJ branch of a given K'–K'' series. The $J'' - 1$ exponent (instead of J'') is a completely arbitrary choice. A second arbitrary choice was to take $\Delta_{obs} > 0$ for the $K = +2 \leftarrow -1$ Q branch in Figure 6 (which was the first long series of doublets to be examined theoretically here).

The two assumptions in the previous paragraph exhaust the arbitrary sign choices, so we must now determine Δ_{obs} signs for the remaining four branches that are consistent with these choices. To accomplish this we carried out fits covering all $2^4 = 16$ possible sign combinations, and then chose the "best sign combination" using two intuitive (but unproven) criteria: (i) the standard deviation of the best sign combination should be among the lowest of the 16 possibilities, and (ii) the spin-rotation constants should not take values above 10 or 15 kHz. Table III shows, as an example, the 16 possibilities for fits floating six constants, i.e., three $A_{ij}^{(1)}$ and three $A_{ij}^{(2)}$ constants (using a nearly final data set). The best sign combination from this table is clearly in the column labeled Sign14, and turns out to require the splittings for three branches to be negative. In all subsequent fits of our data set we use the Sign14 combination from Table III. Even though residuals from this sign combination are quite satisfying, it must be remembered that these signs have not been determined experimentally, and they may have to be modified if contradictory experimental measurements appear.

B. Least-squares fits of the observed hyperfine doublets

Table IV gives a list of the 55 observed doublet splittings (in kHz) used to determine the torsionally mediated nuclear-spin–overall-rotation constants $A_{ij}^{(1,2)}$ in Eqs. (21) and (22) from our least-squares fits, together with residuals calculated using constants from two of these fits. The transitions belong to five relatively long branches, with J values spanning the range from 13 to 34. Many doublet splittings were measured more than once, and in those cases an average was taken (including cases where the same splitting was measured in both laboratories).

Figure 7 is a reduced energy level diagram in which values of $E(J,K) - E(J,K=0)$ for the $|K| \leq 3$ ^{tr}E states of methanol[18] are plotted against J for given K. This type of plot puts all $E(J,K=0)$ levels on a horizontal line with ordinate $E(J,0) - E(J,K=0) = 0$ and illustrates the fact that the K-spacings vary rather slowly with J. Each of the five measured branches is indicated schematically on the left of Figure 7 by a solid vertical arrow, which is color coded to match the symbols in Figure 6.

Figure 6(a) is a graphical display of results from a fit to Eq. (28) where only three $A_{ij}^{(2)}$ coefficients were floated (called FitA$^{(2)}$ here). Symbols represent the measured splittings and solid curves represent splittings calculated using constants from the fit, as given in Table V. Only two data points out of 57 measurements were excluded from the fit. Note also that analysis of the torsion-rotation spectrum[12] only goes up to $J = 30$. Thus, all hyperfine splittings calculated for $J \geq 31$ in Table IV and Figure 6(a) must be treated with caution, since they come from expectation values of spin-rotation operators containing the torsional factors $e^{\pm 2i\alpha}$ over torsion-rotation wavefunctions obtained only by extrapolation.

FitA$^{(2)}$ has a standard deviation of 0.595 kHz, which we feel represents a fit to our experimental measurement precision. As can be seen from Table V, the constant $(1/2)(A_{xx}^{(2)} + A_{yy}^{(2)})$ is not well determined. It turns out, in fact, that a two-parameter fit with $(1/2)(A_{xx}^{(2)} + A_{yy}^{(2)}) = 0$ gives the same standard deviation of 0.594 kHz and gives values for $(1/2)(A_{xx}^{(2)} - A_{yy}^{(2)})$ and $A_{xy}^{(2)}$ that agree with those for FitA$^{(2)}$ in Table V to within 1.3%. Since we know of no theoretical reason to expect $(1/2)(A_{xx}^{(2)} + A_{yy}^{(2)}) \equiv 0$, we speculate that including in the fit doublet splittings from other branches (particularly from excited torsional states) might lead to a better determination of this small parameter.

We also carried out a fit using the corresponding three $A_{ij}^{(1)}$ parameters (called FitA$^{(1)}$). Residuals from this fit are given in the last column of Table IV, constants are given in Table V, and a graphical display of the results is given in Figure 6(b). This fit, which uses spin-rotation operators containing the factors $e^{\pm i\alpha}$, has a standard deviation of 2.34 kHz. FitA$^{(1)}$ is clearly inferior to FitA$^{(2)}$, but this

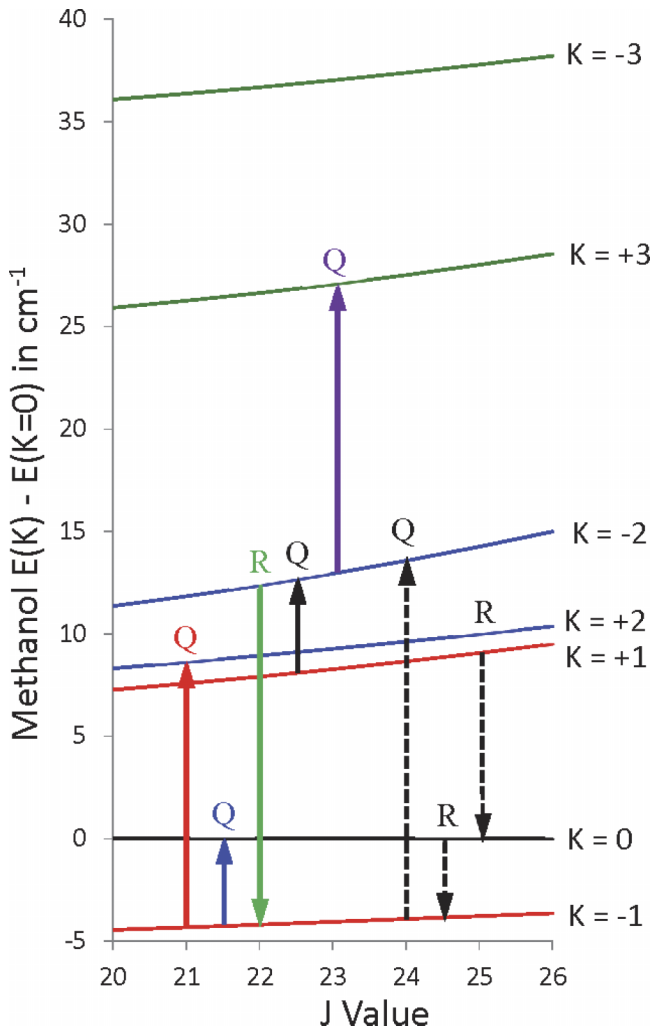

FIG. 7. Overview of the signed-K E-species energy levels of methanol and of transitions between them that have been examined experimentally. The energy of each J level in the $K = 0$ series is placed on the abscissa (i.e., these levels are given energy zero in the figure). Energies of J levels in the other K series are plotted relative to the energy for that J value in the $K = 0$ series. The five solid (and color-coded) arrows on the left correspond to the five branches shown in Figure 6, whose doublets were used in the least-squares fits of Tables IV and V. The three dashed black arrows on the right correspond to branches for which doublet splittings could not be detected (see Figures 5 and 9). Examples of observed lines from three of the branches in this figure are illustrated in Figures 1 and 3.

observation must be treated with caution, because (as pointed out above) the quantum number coverage of the present data set is limited. It is thus conceivable (though we believe not probable) that FitA$^{(2)}$ could be significantly degraded and FitA$^{(1)}$ could be significantly improved when hyperfine splittings from excited torsional states are included in a fit where more spin-rotation constants are floated.

Figure 8 presents an energy level diagram for $-3 \leq K \leq +3$ levels with J = 19, 20, and 21, as calculated from the FitA$^{(2)}$ parameters in Table V. One question that arises at this point is how closely these precisely calculated energy level splittings resemble those in Figures 5 and S-1. There are in fact two significant differences.

The first difference concerns the magnitude of the doublet splittings in the various levels. In Figure 5, which is taken from early attempts[1] to understand the new experimental observations, and in Figure S-1, which depicts results from the simple model calculation in Section IV E, doublet splittings have essentially the same magnitude for all levels. In Figure 8, the calculated doublet splittings shown at the bottom vary with K by a factor of 1000. The variation with J within a given K stack is much smaller, however, particularly when the expected increase with $(J + 1/2)$ is removed from the J variation. As interpreted using the present model, the variation with K results from changes in the complicated torsional and rotational basis-function mixing in the methanol ^{tr}E eigenfunctions,[17] which then leads to changing contributions to the hyperfine energies from the two most important torsionally mediated nuclear-spin–overall-rotation hyperfine interaction terms shown in Table V.

The second difference concerns the symmetry labels of the energy levels. In Figures 5 and S-1, these labels alternate rather consistently as both J and K change. In Figure 8, the J alternation is preserved, but the K alternation breaks down for $K \geq 0$. In spite of this breakdown in symmetry species alternation, the doublet splittings and selection rules for allowed transitions obtained in the present work are still able to fit the experimental measurements. The fact that the symmetry label alternation with J is preserved suggests that a-type transitions within a given K stack will never exhibit observable doublet splittings, i.e., will never exhibit splittings larger than a few kilohertz in the J range of the current methanol measurements.

A second question arises when looking at Figure 8, namely, does it show us the way to predict the size of doublet splittings in other molecules? Clearly, large doublet splittings will not be observable when the upper and lower states involved in the transition have only small doublet splittings themselves. The following two types of information are required to calculate the analog of Figure 8 for other molecules. (i) Approximate values for the three torsional parameters F, V_3, ρ and for the four rotational constants A, B, C, D_{ab} are needed to estimate basis set compositions of the ^{tr}E states of the molecule. These seven parameters can all be obtained with an accuracy sufficient for rough predictive purposes from standard quantum chemical calculations. (ii) Values for the hyperfine parameters A_{ij} are needed to provide coefficients for the spin-rotation interaction terms in Eq. (28), or more generally in Eq. (20). For rough predictive purposes, it may be simplest to give a few of the $A_{ij}^{(1)}$ or $A_{ij}^{(2)}$ coefficients random values of the order of 1 kHz (perhaps scaled down a bit by appropriate rotational constant ratios)[13] and then see what the calculation produces. For more accurate theoretical estimates of these parameters see Section VI D.

C. Predicted hyperfine splittings for transitions not included in the fit

Other transitions for which predicted hyperfine splittings are of interest fall into two categories. The first category contains the E-species transitions observed as narrow Lamb-dip singlets in the present measurement campaign. These transitions have J and K values similar to those

TABLE V. Phenomenological spin-rotation constants in kHz for the I = ½ nuclear spin state associated with ^{tr}E levels in methanol, as determined from least-squares fits of doublet splittings.

Parameter[a]	Matrix element[b]	FitA$^{(2)}$[c]	Theory[d]	FitA$^{(1)}$[e]	Theory[f]
$(1/2)\,(A_{xx}{}^{(n)}+A_{yy}{}^{(n)})$	$\langle J_x{}^2+J_y{}^2\rangle^{(n)}/J(J+1)$	0.0078(79)	0.0018	−0.023(25)	0.038
$(1/2)\,(A_{xx}{}^{(n)}-A_{yy}{}^{(n)})$	$\langle J_x{}^2-J_y{}^2\rangle^{(n)}/J(J+1)$	1.740(27)	1.664	2.574(49)	0.029
$A_{xy}{}^{(n)}$	$i\,\langle J_xJ_y+J_yJ_x\rangle^{(n)}/J(J+1)$	1.547(29)	1.665	2.621(65)	−0.017
σ[g]		0.59		2.34	

[a]Linear combinations of hyperfine interaction constants occurring after slight rearrangement of the Hamiltonian expressions in Eqs. (21)–(23) and of the doublet splitting expression in Eq. (28). Values for these parameters in kHz for n = 1 and 2 are shown on the right side of the table.
[b]Expectation values that are multiplied by the parameters on their left in Eqs. (23) and (28). These matrix element symbols are defined in Eq. (24).
[c]Parameters from a least-squares fit called FitA$^{(2)}$, in which $A_{zz}{}^{(2)}$ and all $A_{ij}{}^{(1)}$ in Eq. (28) were fixed at 0. Type A standard errors[19] are in parentheses. Observed doublet splittings and least-squares residuals from the fit are shown in Table IV. These parameters can be used in conjunction with Table II to calculate the $J_K = 20_{-2}$, 21_{-2} and 21_{-1} doublet splittings shown in Figure 8.
[d]Theoretical values taken from Table VI of Ref. 4, assuming that $A_{xx}{}^{(2)} = c_{xx}{}^2$, $A_{yy}{}^{(2)} = c_{yy}{}^2$, and $A_{xy}{}^{(2)} = -c_{xy}{}^2$ (see Section VI D). Note the good agreement with the FitA$^{(2)}$ parameters.
[e]Parameters from a least-squares fit called FitA$^{(1)}$, in which $A_{zz}{}^{(1)}$ and all $A_{ij}{}^{(2)}$ in Eq. (28) were fixed at 0. Type A standard errors[19] are in parentheses. Observed doublet splittings and least-squares residuals from the fit are shown in Table IV.
[f]Theoretical values taken from Table VI of Ref. 4, assuming that $A_{xx}{}^{(1)} = c_{xx}{}^1$, $A_{yy}{}^{(1)} = c_{yy}{}^1$, and $A_{xy}{}^{(1)} = c_{xy}{}^1$ (see Section VI D). Note the poor agreement with the FitA$^{(1)}$ parameters.
[g]Standard deviation of each fit in kHz.

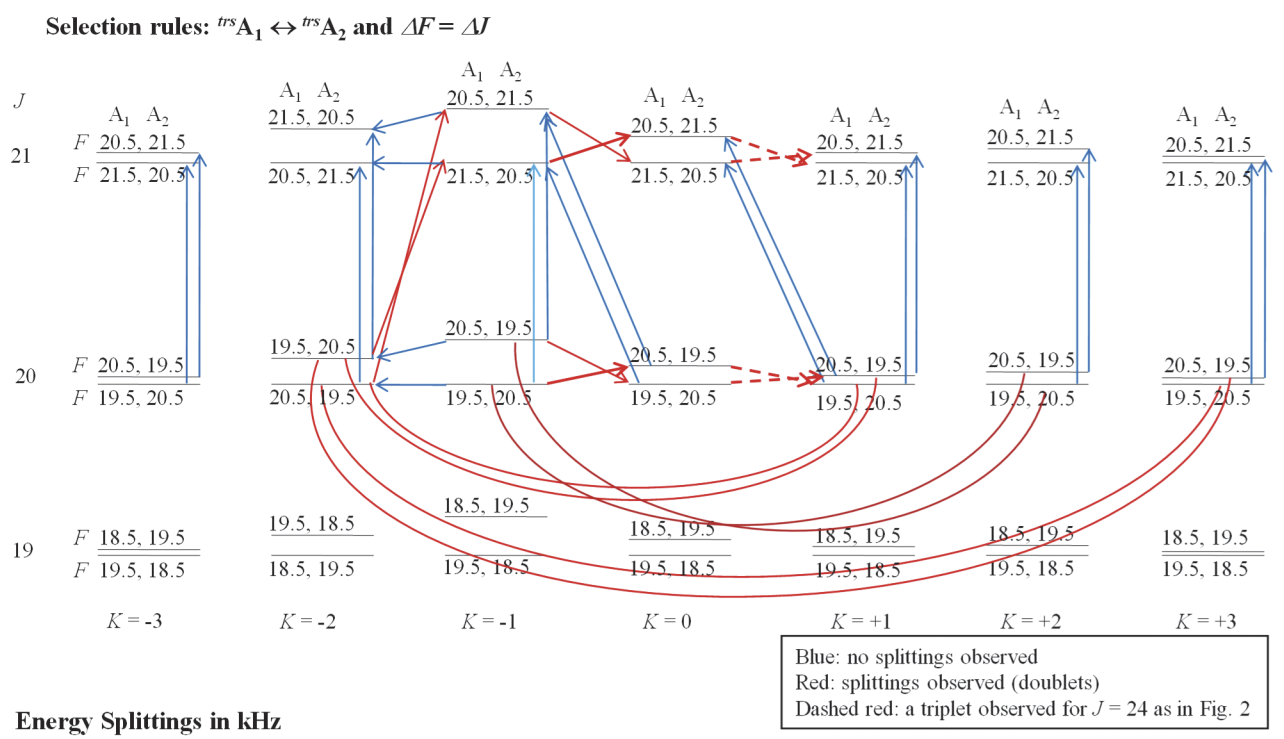

Energy Splittings in kHz

J	K = -3	-2	-1	0	+1	+2	+3
21	0.716	21.572	34.176	18.007	1.274	3.474	0.031
20	0.563	19.450	32.723	16.307	1.196	3.049	0.029
19	0.438	17.290	31.246	14.630	1.116	2.565	0.025

FIG. 8. A diagram analogous to Figures 5 and S-1, drawn with J = 19, 20, and 21 energy levels calculated from FitA$^{(2)}$ in Tables IV and V. This diagram gives a pictorial representation of the final theoretical results of this paper. Calculated values for the hyperfine splittings are indicated in the lower part of the figure. The splitting of the ^{tr}E levels by proton-spin–overall-rotation hyperfine interaction is drawn (but not to scale) in the upper part. J, F, and $^{trs}\Gamma$ symmetry labels are indicated for each level. The pairs of hyperfine levels with the smallest relative splittings in Figure S-1 are drawn here as single (unresolved) levels (e.g., the ^{trs}A$_1$; F = 20.5 and ^{trs}A$_2$; F = 21.5 levels shown in the upper left corner). ^{trs}A$_1$ ↔ ^{trs}A$_2$ and $\Delta F = \Delta J$ selection rules lead to the red and blue transitions shown, which are color coded as in Figure 5, so that red transitions exhibit large doublet splittings, while blue transitions exhibit no measureable doublet splittings. The K = +1 ← 0 dashed lines do not occur as doublets (see Figure 2 and text) and were not included in the fits. This figure is on the whole quite similar to Figure 5, but a number of differences from some of the initial working assumptions in Figure 5 also occur (see text).

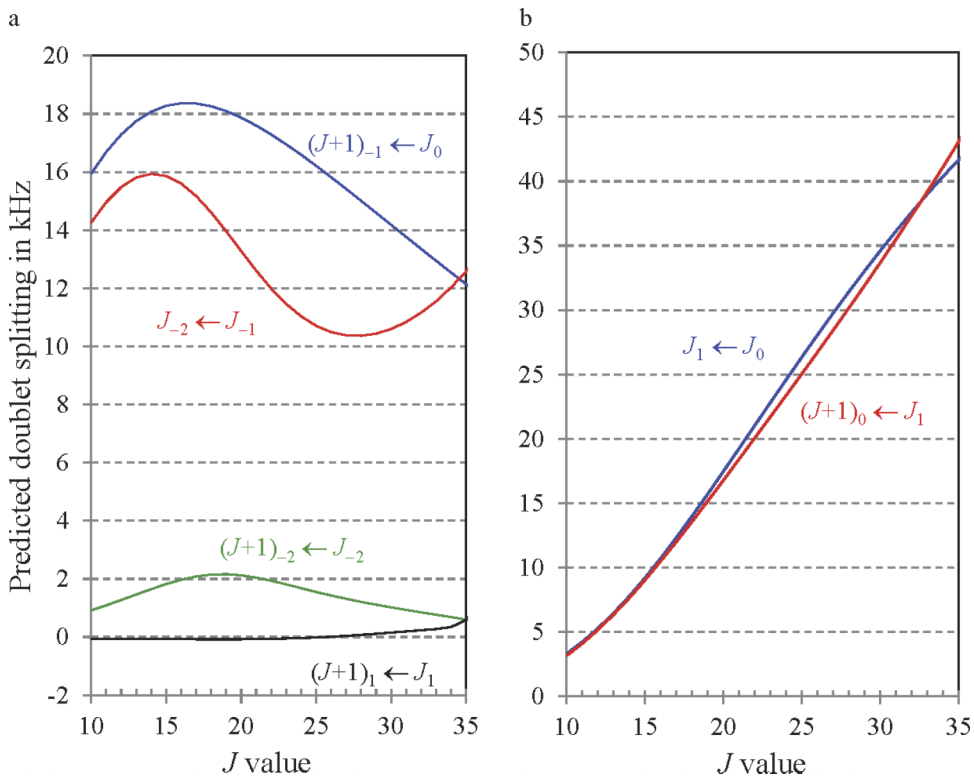

FIG. 9. (a) Predicted splittings for four branches where no splittings were observed in the Lamb-dip spectra (see Figures 1(c) and 1(d), and the blue arrows in Figure 5). These branches do not provide doublet-splitting data for the least-squares fit, but they do provide support for the present theoretical interpretation, since this figure predicts that splittings will be too small to be seen in those branches (see text). (b) Predicted splittings for one R and one Q branch involving $K = 0 \leftrightarrow 1$ transitions. The R-branch measurements show no splittings, but they extend only to $J = 13$, where predicted splittings are $\leq$8 kHz, i.e., are still too small to be seen with our present Lamb-dip spectrometers. The $J = 24$ Q-branch line shown in Figure 2 has a triplet structure with splittings between adjacent components of about 20 kHz. While we do not understand triplet splittings at present, this observed 20 kHz splitting is of the same order of magnitude as the 25 kHz splitting predicted here for the $J = 24$ Q-branch line.

of the observed doublets, so if the present formalism is correct, it should "predict" very narrow doublet splittings for them. The second category contains E-species lines whose hyperfine structure was analyzed in Ref. 4. These lines have quite low J values, and for that reason splittings from the present model (which decrease approximately linearly with J) are expected to make only minor contributions to the total hyperfine energies.

Figure 9(a) shows the doublet splittings predicted from the constants of FitA$^{(2)}$ in Table V for four branches where no splittings are observed experimentally. It can be seen that predicted splittings for the $\Delta K = 0$ R branches are less than 2 kHz. For both $|\Delta K| = 1$ branches, the predicted splittings are all between 10 and 19 kHz. Since doublet splittings of these magnitudes cannot be resolved for methanol by either Lamb-dip spectrometer available for the present work, these small predicted splittings represent an additional type of good agreement between the present theory and the experimental observations. Two of these branches are illustrated in Figure 7 by dashed arrows.

Figure 9(b) shows the doublet splittings predicted from the constants of FitA$^{(2)}$ for the $K = 0 \leftarrow 1$ R branch and the $K = 1 \leftarrow 0$ Q branch shown in Figure 5. Splittings were not observed in the R branch. This is in agreement with theory, since present measurements only extend to $J'' = 13$, and splittings for $J'' \leq 13$ are calculated in Figure 9(b) to be less than 7 kHz. This branch is shown as a dashed arrow in Figure 7. The $J = 24$ Q-branch line in the $K = 1 \leftarrow 0$ series is seen in Figure 2 to be a triplet. As already indicated, we do not at present have a theoretical explanation for triplet patterns, but the calculated splitting of about 25 kHz for this line in Figure 9(b) is at least not totally inconsistent with the size of the splittings seen in Figure 2. This poorly understood $K = 1 \leftarrow 0$ Q branch is not shown in Figure 7.

Table I of Ref. 4 contains E-species transitions with J from 2 to 6 of the $K = +2 \leftarrow +1Q$ branch. Contributions to the splittings of these transitions calculated using the FitA$^{(2)}$ parameters in Table V are all less than 0.4 kHz for this J range, which is much smaller than the FWHM values of about 15 kHz shown in Figure 7 of Ref. 4. Table I of Ref. 4 also contains the 9_{-1} E $\leftarrow$ 8_{-2} E transition. Figure 6(a) indicates that the torsionally mediated spin-rotation interaction considered here could contribute 17 or 18 kHz to the hyperfine splitting in this transition. It is difficult to make use of this information however, because of the measurement inconsistencies pointed out for this line in Ref. 4.

D. Comparison of spin-rotation parameters from this work and Ref. 4

The two spin-rotation constants ($c_{zz}{}^{0}$ and $c_{zz}{}^{0,h}$) determined from analysis of the experimental data in Table X of Ref. 4 are defined in Eq. (19) there to multiply spin-rotation operators with no dependence on the torsional angle α, so these fitting parameters cannot be compared with our fitting parameters $A_{ij}{}^{(1,2)}$.

On the other hand, the middle column of Table VI of Ref. 4 contains theoretically calculated *ab initio* values for our $A_{ij}{}^{(1,2)}$ parameters. By using Eqs. (2), (S-4), (S-5), and (22) here and Eqs. (6) and (18)–(20) in Ref. 4, it is possible to show, for $n = 1$ or 2, that our $A_{ij}{}^{(n)} = +c_{ij}{}^{n}$ in Ref. 4 when $i = j = x$ or y, and that $A_{xy}{}^{(n)} = (-1)^{n-1}c_{xy}{}^{n}$. These relations lead to the comparisons in Table V. The extremely good agreement between the calculated values

of Ref. 4 and the experimentally determined $A_{ij}^{(2)}$ values here, in contrast to the rather poor agreement with the FitA$^{(1)}$ results, is consistent with our choice of FitA$^{(2)}$ as the correct fit based on its overall standard deviation. This agreement also suggests that quantum chemistry calculations like those in Ref. 4 can be used to obtain good estimates of torsionally mediated spin-rotation coupling constants for other molecules.

VII. CONCLUSION

Conclusions from the present work can be summarized in four remarks. (i) Unexpected splittings were observed in rotational transitions between certain pairs of methanol E states. The splittings are not artifacts because they were observed in two laboratories. (ii) By focusing on torsionally mediated spin-rotation operators, which do not occur in molecules without internal rotation, it was possible to construct a Hamiltonian operator that was able to fit available splittings to better than 1 kHz, i.e., to experimental measurement accuracy. (iii) Because of correlation between various parameters in the effective Hamiltonian, only a small number could be determined in any given least-squares fit. It is therefore possible that the present best fit may not be unique or that it may not accurately reflect the full range of physical interactions involved in the spin-rotation coupling problem in methanol. (iv) The correctness of the final fit selected in the present work is supported by the surprisingly good agreement with *ab initio* results already in the literature.

It should also be noted in this connection that our current model demonstrated considerable predictive power during the course of the present study. For example, an early fit of only the $K = 2 \leftarrow -1$ and $K = 0 \leftarrow -1$ series of $\Delta J = 0$ doublets provided rather good predictions for all the other series of doublet splittings appearing in our final fit. The authors consider this fact to be a second relatively strong argument in favor of the overall validity of the present approach, as well as an argument for the validity of the fitted hyperfine parameters obtained from FitA$^{(2)}$. Furthermore, the present model is capable of fitting the rather complicated J and K variation of the 55 doublet splittings shown in Figure 6 using only three adjustable hyperfine parameters, which gives a respectable ratio of 18 splittings/parameter. (This ratio does not count, of course, the very large number of torsion-rotation parameters adjusted in the published fit of Ref. 12, which we used here without change.) Taken as a whole, the various remarks above suggest that the FitA$^{(2)}$ parameters in Table V should remain fairly stable when data from excited torsional states are added to the analysis.

It is already known from preliminary measurements of the splittings in torsionally excited states of methanol that triplet and quartet patterns become more prevalent. What is not known is whether the relatively simple ideas in Section S-III[17] will permit our effective Hamiltonian in its present form (or with only slight modifications) to fit excited-state data. Performing such fits should be relatively straightforward, however, since $v_t = 1$ and $v_t = 2$ transitions were included in the analysis of Ref. 12, and good torsion-rotation eigenfunctions for these two excited torsional states are therefore available. The authors wish to pursue fits of data with an enlarged v_t range, since such fits should provide a stricter test of the model and should also break some of the correlations mentioned above and therefore provide a more physically meaningful set of parameters.

Finally, we might try to guess what other molecules will exhibit splittings similar to those observed in methanol. The simple model introduced in Section IV E suggests that for analogous large hyperfine splittings to be present, adjacent K values should belong to rather different asymmetric-rotor vs torsion-Coriolis-interaction coupling cases. The hyperfine splittings in Figure 8 show that for the ground state of methanol considered here only a few adjacent K values satisfy this requirement. It seems likely that good candidate molecules for large torsionally mediated spin-rotation hyperfine splittings will satisfy three criteria. (i) Their $+K/-K$ torsional splittings in ^{tr}E levels will be comparable to $(B - C)J$ values for thermally and instrumentally accessible J and K ranges. (ii) They will have a large value of ρ, so that a relatively large change in coupling case can occur from one K value to the next. (iii) They will have relatively large rotational constants, since one theoretical derivation of spin-rotation hyperfine constants[13] makes them directly proportional to the rotational constants. From a chemical point of view, methylmercaptan and acetaldehyde, or even the more complicated molecule $CH_3{}^{15}NH_2$ (with two LAMs, but no ^{14}N quadrupole splittings), come to mind.

ACKNOWLEDGMENTS

L.H.X. acknowledges the financial support of a Discovery Grant from the Natural Sciences and Engineering Research Council of Canada. S.P.B. and G.Yu.G. acknowledge State Project No. 0035-2014-009 from the Russian Federal Agency for Science and Innovation (FASI) for support.

[1]G. Yu. Golubiatnikov, S. P. Belov, and A. V. Lapinov, Paper MF04 (2013); S. P. Belov, A. V. Burenin, G. Yu. Golubiatnikov, and A. V. Lapinov, Paper FB07 (2013); in *International Symposium on Molecular Spectroscopy* (The Ohio State University, 2013).
[2]J. E. M. Heuvel and A. Dymanus, J. Mol. Spectrosc. **45**, 282 (1973).
[3]J. E. M. Heuvel and A. Dymanus, J. Mol. Spectrosc. **47**, 363 (1973).
[4]L. H. Coudert, C. Gutlé, T. R. Huet, J.-U. Grabow, and S. A. Levshakov, J. Chem. Phys. **143**, 044304 (2015).
[5]G. Yu. Golubiatnikov, S. P. Belov, I. I. Leonov, A. F. Andriyanov, I. I. Zinchenko, A. V. Lapinov, V. N. Markov, A. P. Shkaev, and A. Guarnieri, Radiophys. Quantum Electron. **56**, 599 (2014) [IzvestiyaVuzov Radiofizika **56**, 666 (2013) (in Russian)].
[6]Note that certain commercial products are mentioned when specifying the experimental setups used in the present study. In no case does such identification imply recommendation or endorsement by the National Institute of Standards and Technology nor does it imply that the products are necessarily the best available for the purpose.
[7]V. P. Kochanov, S. P. Belov, and G. Yu. Golubiatnikov, J. Quant. Spectrosc. Radiat. Transfer **149**, 146 (2014).
[8]E. A. Alekseev, V. V. Ilyushin, and A. A. Mescheryakov, Radio Phys. Radio Astron. **19**, 364 (2014) (in Russian).
[9]G. Cazzoli, C. Puzzarini, and A. V. Lapinov, Astrophys. J., Lett. **592**, L95 (2003).
[10]E. A. Alekseev, R. A. Motiyenko, and L. Margulès, Radio Phys. Radio Astron. **3**, 75 (2012).

[11]A. V. Lapinov, S. A. Levshakov, M. G. Kozlov, G. Yu. Golubiatnikov, S. P. Belov, A. F. Andriyanov, A. P. Shkaev, I. I. Agafonova, and I. I. Zinchenko, Vestnik RFFI. **#1**(73), 111 (2012) (in Russian).
[12]L.-H. Xu, J. Fisher, R. M. Lees, H. Y. Shi, J. T. Hougen, J. C. Pearson, B. J. Drouin, G. A. Blake, and R. Braakman, J. Mol. Spectrosc. **251**, 305 (2008).
[13]C. H. Townes and A. L. Schawlow, *Microwave Spectroscopy* (McGraw-Hill, 1955).
[14]J. T. Hougen, I. Kleiner, and M. Godefroid, J. Mol. Spectrosc. **163**, 559 (1994).
[15]M. Tudorie, L. H. Coudert, T. R. Huet, D. Jegouso, and G. Sedes, J. Chem. Phys. **134**, 074314 (2011).
[16]L. H. Coudert and J. C. López, J. Mol. Spectrosc. **239**, 135 (2006).
[17]See supplementary material at http://dx.doi.org/10.1063/1.4954941 for more details on the calculations in this paper.
[18]L.-H. Xu and F. J. Lovas, J. Phys. Chem. Ref. Data **26**, 17 (1997).
[19]B. N. Taylor and C. E. Kuyatt, Guidelines for Evaluating and Expressing the Uncertainty of NIST Measurement Results, 1994, http://physics.nist.gov/TN1297.